A conservative, implicit solver for 0D-2V multi-species nonlinear Fokker-Planck collision equations

Yanpeng Wang[a]**, Jianyuan Xiao** [1a]**, Yifeng Zheng**[c]**, Zhihui Zou**[d]**, Pengfei Zhang**[b]**, Ge Zhuang**[a]

[a]School of Nuclear Sciences and Technology, University of Science and Technology of China, Hefei, 230026, China
[b]School of Physical Sciences, University of Science and Technology of China, Hefei, 230026, China
[c]Institute of Plasma Physics, Chinese Academy of Sciences, Hefei 230031, China
[d]Institute for Fusion Theory and Simulation, School of Physics, Zhejiang University, Hangzhou 310027, China

Abstract.   In this study, we present an optimal implicit algorithm specifically designed to accurately solve the multi-species nonlinear 0D-2V axisymmetric Fokker-Planck-Rosenbluth (FPR) collision equation while preserving mass, momentum, and energy. Our approach relies on the utilization of nonlinear Shkarofsky's formula of FPR (FPRS) collision operator in the spherical-polar coordinate. The key innovation lies in the introduction of a new function named King, with the adoption of the Legendre polynomial expansion for the angular coordinate and King function expansion for the speed coordinate. The Legendre polynomial expansion will converge exponentially and the King method, a moment convergence algorithm, could ensure the conservation with high precision in discrete form. Additionally, post-step projection onto manifolds is employed to exactly enforce symmetries of the collision operators. Through solving several typical problems across various nonequilibrium configurations, we demonstrate the high accuracy and superior performance of the presented algorithm for weakly anisotropic plasmas.

Keywords: Fokker-Planck-Rosenbluth, Conservation, Nonlinear, Weakly anisotropic plasma, Legendre polynomial, King function.

1 Introduction

In plasma physics, the Fokker-Planck collision operator, known as the Fokker-Planck-Rosenbluth[1–4] (FPR) or equivalently the Fokker–Planck–Landau[5] (FPL) operator, is a fundamental tool for describing Coulomb collisions between particles under the assumptions of binary, grazing-angle collisions. This operator is particularly valuable for modeling various plasma systems, including those found in laboratory settings such as magnetic confinement fusion (MCF) and inertial confinement fusion (ICF), as well as in natural environments like Earth's magnetosphere and astrophysical phenomena like solar coronal plasma. When coupled with Vlasov's equation[6] and Maxwell's equations, it provides a comprehensive description of weakly coupled plasma across all collisionality regimes.

The FPR collision operator ensures strict conservation of mass, momentum and energy, while also adhering to the well-established H-theorem[7] , which guarantees that the entropy of the plasma system increases monotonically with time unless the system reaches a thermal equilibrium state. Throughout history, various formulations of the Fokker-Planck collision operator have been developed to suit different computational and theoretical needs. The FPL collision operator employs a direct integral formulation, making it ideal for conservative algorithms and the H-theorem[7] due to its symmetric nature. Conversely, the standard FPR collision operator[1] represents integral relationships using Rosenbluth potentials, which satisfies the Poisson equation in velocity space. The

---

[1]xiaojy@ustc.edu.cn

divergence form of the FPR (FPRD)[2,8,9] collision operator is widely favored in numerical simulations due to its efficiency in fast solvers. Additionally, when employing spherical harmonic expansions, Shkarofsky's formula of the FPR collision operator (FPRS)[3,4] collision operator is often preferred for its computational advantages. These various formulations offer flexibility and efficiency in solving Vlasov-Fokker-Planck (VFP) equation, catering to different computational and theoretical requirements.

Historically, numerous efforts have been dedicated to addressing the numerical solution of the Fokker-Planck collision equation. Thomas[10] and Bell[11] reviewed the different numerical models of Fokker-Planck collision operator for ICF plasma. Cartesian tensor expansions[12–15] (CTE) and spherical harmonic expansions[11,16–20] (SHE), or Legendre polynomial expansions[21–26] when axisymmetric, are employed to handle the Fokker-Planck collision operator, which are considered equivalent to each other[12].

SHE[11,17,22–25] is an crucial method for moderate nonequilibrium plasma when the ratio of average velocity to thermal velocity is not large. As emphasized by Bell[11], the amplitude of each harmonics will decay exponentially at a rate proportional to $l(l + 1)/2$. Even in cases of weak collisions, this $l(l + 1)/2$ leads to strong damping of higher-order spherical harmonics, naturally terminating the expansion. Early studies by Bell[22] and Matte[23] focused on including the first two order harmonics to investigate non-Spitzer heat flow in ICF plasma. Subsequent work by Shkarofsky[24] and Alouani-Bibi[25] extended this approach to higher orders, resulting in the widely used semi-anisotropic collision operator[25]. In recent years, several VFP codes[11,17,27] based on the semi-anisotropic model have been developed. However, effectively calculating the full nonlinear collision operator in the SHE approach remains a challenge[11,17], especially in scenarios involving large mass disparities such as electron-deuterium collisions in fusion plasma. While previous simulations utilizing SHE have adopted the semi-anisotropic model and maintained mass and energy conservation, achieving exact momentum conservation in discrete simulations remains problematic.

Other computational approaches such as meshfree methods[28–31] and finite volume method[32] (FVM) are also employed to solve the Fokker-Planck collision equation. Fast spectral method based on FFT[28–30] or Hermite polynomial expansion[33] has shown rapid convergence of spectral expansion strategy[34] in approximating the FPL collision operator. Additionally, Askari[31] employed a meshfree method using multi-quadric radial basis functions (RBFs) to approximate the solution of the 0D-1V Fokker-Planck collision equation. Taitano et al.[2,9,35–37] carried out systematic studies based on the 0D-2V FPRD collision operator by directly discretizing the collision equation with FVM. They[2] developed an implicit algorithm and overcame the Courant-Friedrichs-Lewy[38] (CFL) condition by utilizing a second-order BDF2 implicit solver and employing the multigrid (MG) method[39] in Jacobian-Free Newton-Krylov (JFNK)[39] solver. Furthermore, by normalizing the velocity space to the local thermal velocities of each species individually[40], works in Ref.[9] developed a discrete conservation strategy that utilizes nonlinear constraints to enforce the continuum symmetries of the collision operator. However, those approaches did not take advantages of Coulomb collisions, similar to SHE[11], to reduce the number of meshgrids when there are no distinguishing asymmetries in the velocity space.

The challenge of employing SHE[11] and previous meshfree[31] approaches lies in embedding discrete conservation laws within the numerical scheme. According to manifold theory[41], maintaining a small local error through post-step projection onto manifolds preserves the same convergence rate. Therefore, backward error analysis[42,43] has become a

crucial tool for understanding the long-term behavior of numerical integration methods and preserving conservation properties in the numerical scheme.

In this study, our objective is to address the full nonlinearity, discrete conservation laws, and the temporal stiffness challenge of the 0D-2V axisymmetric multi-species FPRS collision equations within the SHE approach. Similar to previous works in Ref.[9] , we normalize the velocity spaces to the local thermal velocities for all species separately. However, instead of utilizing multigrid (MG) technology as in Ref.[2] , we employ a meshfree[44] approach based on King method (details in Sec. 3.2.1) by introducing a novel shape function named King to overcome the classical CFL condition. To tackle the nonlinear, stiff FPRS collision equations, we propose an implicit algorithm based on Legendre polynomial expansion for the angular coordinate, the King function expansion for the speed coordinate, and the trapezoidal method[34,45] for time integration. Romberg integration[46] is employed to compute kinetic moments with high precision, and backward error analysis[42,43,47] is applied to ensure numerical conservation of mass, momentum, and energy. The H-theorem[7] is satisfied in the discretization scheme and utilized as a criterion for convergence of our algorithm.

The rest of this paper is organized as follows. Sec.2 introduces the FPRS collision equation and its normalization. The discretization of the nonlinear FPRS collision equation is given in Sec.3, encompassing angular discretization and the King method for the speed coordinate. An implicit time discretization and conservation strategies is discussed in Sec.4. The numerical performance of our solver, including accuracy and efficiency, is demonstrated with various multi-species tests in Sec.5. Finally, we conclude our work in Sec.6.

2 The Fokker-Planck-Rosenbluth collision equation

The relaxation of Coulomb collision in a spatially homogeneous multi-species plasma can be described by the FPR collision equation. For species a, the velocity distribution functions $f(\mathbf{v}, t)$, in velocity space $\mathbf{v}$, satisfies:

$$\frac{\partial}{\partial t} f(\mathbf{v}, t) = \mathfrak{C}(\mathbf{v}, t) . \tag{1}$$

The term on the right-hand side represents the FPR collision operator of species a. In this paper, the mass, time, charge, thermal velocity, number density n_a, temperature T_a and permittivity are normalized by the proton mass m_p, characteristic time τ_0, elementary charge $|q_e|$, vacuum speed of light c_0, reference number density $n_0 = 10^{20} \mathrm{m}^{-3}$, practical unit $T_k = \mathrm{keV}$ and permittivity of vacuum ε_0 respectively. The dimensionless form of other quantities is determined based on their correlation with these dimensionless quantities.

The normalization FPR collision equation maintains the same structure as Eq. (1) and $\mathfrak{C}$ can be formulated as:

$$\mathfrak{C}(\mathbf{v}, t) = \sum_{b=1}^{N_s} \mathfrak{C}_{ab} . \tag{2}$$

Here, N_s represents the total number of plasma species and function $\mathfrak{C}_{ab}$ denotes the FPRS collision operator[3,4] for species a colliding with species b, given by:

$$\mathfrak{C}_{ab}(\mathbf{v}, t) = \Gamma_{ab} \left[4\pi m_M F f + (1 - m_M) \nabla_{\mathbf{v}} H \cdot \nabla_{\mathbf{v}} f + \frac{1}{2} \nabla_{\mathbf{v}} \nabla_{\mathbf{v}} G : \nabla_{\mathbf{v}} \nabla_{\mathbf{v}} f \right] . \tag{3}$$

The mass ratio is denoted as $m_M = m_a/m_b$, where symbols m_a and m_b represent the masses of species a and b respectively. Parameter $\Gamma_{ab} = C_\Gamma \times 4\pi \left(\frac{Z_a Z_b}{4\pi m_a} \right)^2 \ln \Lambda_{ab}$ and the dimensionless coefficient $C_\Gamma = \tau_0 \omega_{p_0}^4 / (n_0 c_0^3)$ where $\omega_{p_0} = \sqrt{n_0 q_e^2/(m_p \varepsilon_0)}$. Symbols Z_a and Z_b denote the ionization state of species a and b. Parameter $\ln \Lambda_{ab}$ represents the Coulomb logarithm[48] of species a and b, which is a weak function of the number of particles in the Debye sphere. Function $F = F(\mathbf{v}_b, t)$, representing the distribution function of background species b. Functions H and G denote the Rosenbluth potentials, which are integral operators for the background distribution function F, reads:

$$H(\mathbf{v}) = \int \frac{1}{|\mathbf{v} - \mathbf{v}_b|} F(\mathbf{v}_b, t)\, d\mathbf{v}_b, \quad G(\mathbf{v}) = \int |\mathbf{v} - \mathbf{v}_b|\, F(\mathbf{v}_b, t)\, d\mathbf{v}_b . \tag{4}$$

It is worth noting that, in order to reduce the burden of subscripts in the subsequent sections, the quantities of species a, such as the distribution function f and velocity $\mathbf{v}$, will not include the subscript a in this paper, as commonly practiced[2–4,11,18,23,24,35,49]. Similarly, the quantities of species b, denoted by capital letters, such as the distribution function F, Rosenbluth potentials H and G, are also omitted from including the subscript b.

2.1 Conservation

The FPRS collision operator (give in Eq. (3)) preserves mass, momentum and energy which stems from its symmetries[50]. Using the inner product definition $\langle f, g \rangle_\mathbf{v} = \int g(\mathbf{v}) f(\mathbf{v}) d\mathbf{v}$, these conservation laws can be expressed as follows:

$$\langle 1, \mathfrak{C}_{ab} \rangle_\mathbf{v} = \langle 1, \mathfrak{C}_{ba} \rangle_\mathbf{v} \equiv 0, \tag{5}$$

$$m_a \langle \mathbf{v}, \mathfrak{C}_{ab} \rangle_\mathbf{v} = -m_b \langle \mathbf{v}, \mathfrak{C}_{ba} \rangle_\mathbf{v}, \tag{6}$$

$$m_a \left\langle \frac{\mathbf{v}^2}{2}, \mathfrak{C}_{ab} \right\rangle_\mathbf{v} = -m_b \left\langle \frac{\mathbf{v}^2}{2}, \mathfrak{C}_{ba} \right\rangle_\mathbf{v} . \tag{7}$$

In theory, the FPRS collision operator satisfies the well-known H-theorem. By defining the Boltzmann's entropy of species a, $s_a(t) = -\langle f, \ln f \rangle_\mathbf{v}$, the total entropy of the plasma system can be expressed as $s_s(t) = \sum_a s_a$. According to the H-theorem, the total entropy of an isolated plasma system will monotonically increase over time unless there is no change in total entropy, indicating that all distribution functions are Maxwellian with a common temperature and average velocity.

2.2 Normalization

In fusion plasma, the presence of disparate thermal velocities poses additional challenges, arising from the significant mass discrepancy (*electron*-s*ion* collisions) or energy difference (*deuterium*-*alpha* collisions). This paper specifically focuses on the weakly anisotropic plasmas where the system exhibits no distinguishing asymmetries in the velocity space, such as when the average velocity is significantly smaller than the thermal velocity. Fig. 1 illustrates the distribution function in speed coordinate when bulk flow of plasma is subsonic with a significant discrepancy in thermal velocities. This discrepancy adds complexity to discretizing the speed, particularly when mapping the background species distribution function to the collision species domain. Previous studies[9,40] have shown that normalizing the distribution function by its local thermal velocity (denoted as v_{ath} for species a) can help to mitigate these challenges. This normalization not only alleviates the need for different meshing requirements between multiple species but also
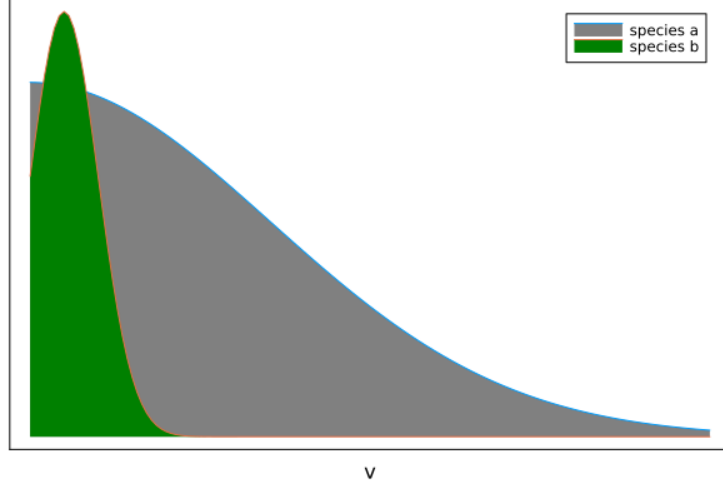
Figure 1: Illustration of the velocity distribution functions in speed coordinate for disparate thermal velocities in a subsonic plasma system.

ensures consistent evolution of thermal velocities over time with respect to temperature changes in distribution functions.

Therefore, we normalize the velocity space with its corresponding local thermal velocity, for species a, reads:

$$\hat{\mathbf{v}} = \mathbf{v}/v_{ath} . \tag{8}$$

Thus, we have $\nabla_{\hat{\mathbf{v}}} = v_{ath}\nabla_{\mathbf{v}}$ and the distribution function can be normalized as follow:

$$\hat{f}(\hat{\mathbf{v}}, t) = n_a^{-1} v_{ath}^3 f(\mathbf{v}/v_{ath}, t) . \tag{9}$$

Therefore, the normalized background distribution function and Rosenbluth potentials can be written as:

$$\hat{F}(\hat{\mathbf{v}}_b, t) = n_b^{-1} v_{bth}^3 F(\mathbf{v}_b/v_{bth}, t), \tag{10}$$

$$\hat{H}(\hat{\mathbf{v}}_{ab}, t) = \frac{v_{bth}}{n_b} H(\mathbf{v}/v_{bth}, t) = \int \frac{1}{\hat{\mathbf{v}}_{ab} - \hat{\mathbf{v}}_b} \hat{F}(\hat{\mathbf{v}}_b, t) \, \mathrm{d}\hat{\mathbf{v}}_b, \tag{11}$$

$$\hat{G}(\hat{\mathbf{v}}_{ab}, t) = \frac{1}{n_b v_{bth}} G(\mathbf{v}/v_{bth}, t) = \int (\hat{\mathbf{v}}_{ab} - \hat{\mathbf{v}}_b) \hat{F}(\hat{\mathbf{v}}_b, t) \, \mathrm{d}\hat{\mathbf{v}}_b, \tag{12}$$

where $\hat{\mathbf{v}}_b = \mathbf{v}_b/v_{bth}$ and $\hat{\mathbf{v}}_{ab} = \mathbf{v}/v_{bth}$.

Hence, the FPRS collision operator (give in Eq. (2)) of species a can be normalized as follows:

$$\hat{\mathfrak{C}}(\hat{\mathbf{v}}, t) = \frac{v_{ath}^3}{n_a} \mathfrak{C}(\mathbf{v}/v_{ath}, t) = \sum_{b=1}^{N_s} \frac{n_b}{v_{bth}^3} \Gamma_{ab} \hat{\mathfrak{C}}_{ab}, \tag{13}$$

where

$$\hat{\mathfrak{C}}_{ab}(\hat{\mathbf{v}}, t) = 4\pi m_M \hat{F}(\hat{\mathbf{v}}_{ab}, t)\hat{f} + C_{\hat{H}} \nabla_{\hat{\mathbf{v}}_{ab}} \hat{H} \cdot \nabla_{\hat{\mathbf{v}}} \hat{f} + C_{\hat{G}} \nabla_{\hat{\mathbf{v}}_{ab}} \nabla_{\hat{\mathbf{v}}_{ab}} \hat{G} : \nabla_{\hat{\mathbf{v}}} \nabla_{\hat{\mathbf{v}}} \hat{f} . \tag{14}$$

Here, m_M is the mass ratio, $\nabla_{\hat{\mathbf{v}}}$ and $\nabla_{\hat{\mathbf{v}}_{ab}}$ are gradients in normalized velocity space $\hat{\mathbf{v}}$ and $\hat{\mathbf{v}}_{ab}$ respectively. The coefficients in Eq. (14) are given by:

$$C_{\hat{H}} = (1 - m_M) v_{bth}/v_{ath}, \quad C_{\hat{G}} = (v_{bth}/v_{ath})^2 /2 . \tag{15}$$

5

The concrete formulation of Eq. (14) is provided in Appendix B. The normalized like-particle collision operator can be derived from Eq. (14) by replacing $\hat{F}$ and $\hat{\mathbf{v}}_{ab}$ by $\hat{f}$ and $\hat{\mathbf{v}}$ respectively, reads:

$$\hat{\mathfrak{C}}_{aa}\left(\hat{\mathbf{v}}, t\right) = 4\pi\hat{f}\hat{f} + \frac{1}{2}\nabla_{\hat{\mathbf{v}}}\nabla_{\hat{\mathbf{v}}}\hat{G} : \nabla_{\hat{\mathbf{v}}}\nabla_{\hat{\mathbf{v}}}\hat{f}. \tag{16}$$

After the applications of Eqs. (8)-(9) and Eq. (13), the finial form of FPR collision equation to be solved numerically in this study is:

$$\frac{\partial}{\partial t}f\left(\hat{\mathbf{v}}, t\right) = \mathfrak{C}\left(\hat{\mathbf{v}}, t\right), \tag{17}$$

where

$$f\left(\hat{\mathbf{v}}, t\right) = \frac{n_a}{v_{ath}^3}\hat{f}\left(\hat{\mathbf{v}}, t\right), \tag{18}$$

$$\mathfrak{C}\left(\hat{\mathbf{v}}, t\right) = \frac{n_a}{v_{ath}^3}\sum\nolimits_{b=1}^{N_s}\frac{n_b}{v_{bth}^3}\Gamma_{ab}\hat{\mathfrak{C}}_{ab}. \tag{19}$$

This paper focuses on the scenario of axisymmetric velocity space. Therefore, Eq. (17) can be referred to as the 0D-2V FPRS collision equation. It is important to note that the fully normalized form of both the velocity space and the objective function, such as $\hat{f}(\hat{\mathbf{v}})$, is utilized to derive $\mathfrak{C}\left(\hat{\mathbf{v}}, t\right)$, while the time derivative employs a semi-normalized form only on the velocity space, such as $f\left(\hat{\mathbf{v}}, t\right)$, rather than $\hat{f}(\hat{\mathbf{v}}, t)$ used by Taitano[9].

The utilization of this semi-normalized equation (17) can eliminate the non-inertial terms[9] and simplify the complexity of the FPRS collision equation. The successful implementation of this approach relies on the utilization of the King method introduced in Sec. 3.2.1, in combination with the time block technique (TBT) detailed in Sec. 4.1.1. The specific implementation in implicit algorithms is provided in the main procedure described by Algorithm 7. In order to develop an effective algorithm, we make the assumption that the distribution function, $f(\hat{\mathbf{v}}, t)$, is a smooth function in the velocity space. It is reasonable that the Coulomb collisions always tends to eliminate the fine structures of the distribution function[11].

3 Discretization of the nonlinear FPRS collision equation

In this study, we adopt a meshfree approach[44] (requiring field nodes) for discretizing the 0D-2V axisymmetric FPRS collision operator within a spherical-polar coordinate in velocity space. The SHE[12,51] method is employed to discretize the angular coordinate of the distribution function. Subsequently, the King function expansion (KFE) method, presented in Sec. 3.2.1, is utilized to the speed coordinate. Based on this framework of SHE together with KFE, a moment convergence algorithm is developed for solving the 0D-2V FPRS collision equation represented by Eq. (17).

3.1 Angular discretization

We opt for the SHE[12,51] method (utilizing Legendre polynomial expansions[1,23–26,52] when the velocity space is axisymmetric) to analytically adapt the velocity-space discretization in angular coordinate. Unlike previous studies[11,18,53] employing the semi-anisotropic model, we will maintain the full nonlinearity of the FPRS collision operator for all species.

3.1.1 Legendre polynomial expansions

The normalized distribution function of species a is described by the real function $\hat{f}(\hat{v}, \theta, t)$ in axisymmetric systems, which can be expanded using Legendre polynomials in normalized velocity space $\hat{\mathbf{v}}(\hat{v}, \theta)$. It can be expressed as:

$$\hat{f}(\hat{v}, \mu, t) = \sum_{l=0}^{\infty} \hat{f}_l(\hat{v}, t) P_l(\mu) . \tag{20}$$

Here, $\hat{v} = |\mathbf{v}|/v_{ath}$, $\mu = \cos\theta$ and $0 \leq \theta < \pi$ when choosing the symmetric axis to be the direction z with base vector $\mathbf{e}_z$. The function $P_l(\mu)$ represents the lth-order Legendre polynomials. For the sake of convenience, we will henceforth denote Eq. (20) as the SHE in axisymmetric velocity space. The calculation for the lth-order normalized amplitude $\hat{f}_l(\hat{v}, t)$ can be obtained through the inverse transformation of Eq. (20) as follows:

$$\hat{f}_l(\hat{v}, t) = \frac{1}{(N_l)^2} \int_{-1}^{1} \hat{f}(\hat{v}, \mu, t) P_l(\mu) \mathrm{d}\mu, \tag{21}$$

where $N_l = \sqrt{(2l+1)/(4\pi)}$, representing the normalization coefficient in spherical harmonics[54].
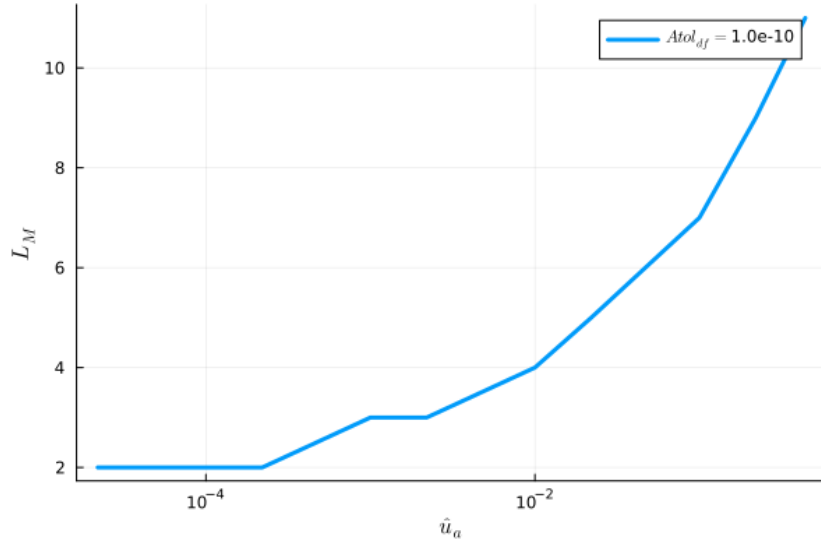

Figure 2: Convergence of SHE for drift-Maxwellian distribution: l_M as a function of $\hat{u}_a$ when $Atol_{df} = 10^{-10}$.

Due to exponential decay of the lth-order amplitude at a rate proportion to $l(l+1)/2$, as stated in Ref.[11] , there is a natural termination to the expansions. Thus, the function $\hat{f}(\hat{v}, \mu, t)$ is represented by a finite set of amplitudes $\hat{f}_l(\hat{v}, t)$, which are dependent on time t and normalized speed $\hat{v} \equiv |\hat{\mathbf{v}}|$. The series in Eq. (20) can be truncated at a maximum order, denoted as l_M, under the specified condition that $max|\hat{f}_l(\hat{v}, t)| \leq Atol_{df}$. Here, $l_M \in \mathbb{N}$ and the subscript M is short for "max". The convergence of SHE for drift-Maxwellian distribution is depicted in Fig. 2. It shows that l_M is monotonic function of $\hat{u}$ when $\hat{u} \leq 0.5$. For example with $\hat{u}_a \leq 2.2 \times 10^{-3}$ and $Atol_{df} = 10^{-10}$, it leads to a maximum order, $l_M = 3$.

Eq. (21) can be computed by utilizing Gaussian quadrature[34] , which can be reformulated as:

$$\hat{f}_l\left(\hat{v}, t\right) = \sum_{\beta=1}^{l_{M_1}} w_{\mu_\beta} P_l(\mu_\beta) \hat{f}\left(\hat{v}, \mu_\beta, t\right) + \mathcal{O}(Atol_{df}), \quad l = 0, 1, 2, \cdots, l_M, \tag{22}$$

where

$$l_{M_1} = l_M + 1. \tag{23}$$

The Gauss-Legendre abscissas will used as the field nodes for the polar angle coordinate μ. The node μ_β represents the βth roots of the Legendre polynomial $P_l(\mu)$, out of a total of l_{M_1} roots. The associated weight w_{μ_β} is computed using Fornberg's algorithm[55] .

3.1.2 Rosenbluth potentials

Similar to Eq. (20), the normalized distribution function of the background species b, can be expended as follows:

$$\hat{F}\left(\hat{v}_b, \mu, t\right) = \sum_{L=0}^{\infty} \hat{F}_L\left(\hat{v}_b, t\right) P_L\left(\mu\right). \tag{24}$$

With a maximum truncated order, L_M, the Lth-order normalized amplitude can be formulated as:

$$\hat{F}_L\left(\hat{v}_b, t\right) = \sum_{\beta=1}^{L_{M_1}} w_{\mu_\beta} P_L(\mu_\beta) \hat{F}\left(\hat{v}_b, \mu_\beta, t\right) + \mathcal{O}(Atol_{df}), \tag{25}$$

where $L_{M_1} = L_M + 1$. Here, we utilize L rather than l because $\hat{F}$ and $\hat{f}$ typically exhibit distinct convergence rates in angular coordinate. The maximum order of angular coordinate during collisions between species a and species b will be denoted as $l_{max} = \max\left(l_M, L_M\right)$. Additionally, we will disregard the truncation error terms from this point onward.

In a similar manner, the normalized Rosenbluth potentials of species a, as described by equations (11)-(12) due to the presence of background species b, can also be represented in an expanded form, reads:

$$\hat{H}\left(\hat{v}_{ab}, \mu, t\right) = 4\pi \sum_{L=0}^{L_M} \hat{H}_L\left(\hat{v}_{ab}, t\right) P_L\left(\mu\right), \tag{26}$$

$$\hat{G}\left(\hat{v}_{ab}, \mu, t\right) = 4\pi \sum_{L=0}^{L_M} \hat{G}_L\left(\hat{v}_{ab}, t\right) P_L\left(\mu\right). \tag{27}$$

Here, $\hat{v}_{ab} = |\mathbf{v}|/v_{bth}$. The coefficient 4π stems from the definitions represented by Eqs. (30)-(31). The Lth-order amplitudes of $\hat{H}$ and $\hat{G}$ can be computed in the following integral form:

$$\hat{H}_L\left(\hat{v}_{ab}, t\right) = \frac{1}{2L+1} \frac{1}{\hat{v}_{ab}} \left(I_{L,L} + J_{L+1,L}\right), \tag{28}$$

$$\hat{G}_L\left(\hat{v}_{ab}, t\right) = \frac{1}{2L+1} \frac{1}{\hat{v}_{ab}} \left(\frac{I_{L+2,L} + J_{L+1,L}}{2L+3} - \frac{I_{L,L} + J_{L-1,L}}{2L-1}\right). \tag{29}$$

Here, $I_{i,L}$ and $J_{i,L}$ represent the functionals of the normalized background distribution function $\hat{F}_L(\hat{v}_b, t)$, following a similar approach as Shkarofsky et al.[4,13], reads:

$$I_{i,L}(\hat{v}_{ab}, t) = I_i\left[\hat{F}_L\right] = \frac{1}{(\hat{v}_{ab})^i} \int_0^{\hat{v}_{ab}} (\hat{v}_b)^{i+2} \hat{F}_L(\hat{v}_b, t)\, d\hat{v}_b, \quad i = L, L+2, \tag{30}$$

$$J_{i,L}(\hat{v}_{ab}, t) = J_i\left[\hat{F}_L\right] = (\hat{v}_{ab})^i \int_{\hat{v}_{ab}}^\infty \frac{\hat{v}_b^2}{(\hat{v}_b)^i} \hat{F}_L(\hat{v}_b, t)\, d\hat{v}_b, \quad i = L-1, L+1. \tag{31}$$

The aforementioned definitions do not include the coefficient 4π, which arises from the use of spherical-polar coordinates in velocity space. The Jacobian $(\hat{v}_b)^2$ used in speed integrals, such as Eqs. (30)-(31), and the subsequent definition of kinetic moment represented by Eq. (38), also stems from the application of spherical-polar coordinates in velocity space.

3.1.3 FPRS collision spectrum equation

Similar to the expansion of $\hat{f}(\hat{\mathbf{v}})$ (give in Eq. (20)), the normalized FPRS collision operator (13) can also be expanded based on the Legendre polynomials, reads:

$$\hat{\mathfrak{C}}(\hat{\mathbf{v}}, t) = \sum_{l=0}^{l_M} \hat{\mathfrak{C}}_l(\hat{v}, t) P_l(\mu). \tag{32}$$

The lth-order amplitude of normalized multi-species nonlinear FPRS operator of species a is given by:

$$\hat{\mathfrak{C}}_l(\hat{v}, t) = \sum_{b=1}^{N_s} \frac{n_b}{v_{bth}^3} \Gamma_{ab} \hat{\mathfrak{C}}_{lab}. \tag{33}$$

Function $\hat{\mathfrak{C}}_{lab}$ represents the lth-order amplitude of normalized FPRS collision operator for species a colliding with species b, which can be expressed as:

$$\hat{\mathfrak{C}}_{lab}(\hat{v}, t) = \sum_{\beta=1}^{l_{M_1}} w_{\mu_\beta} P_l(\mu_\beta) \hat{\mathfrak{C}}_{ab}(\hat{v}, \mu_\beta, t). \tag{34}$$

Function $\hat{\mathfrak{C}}_{ab}$ depends on $\hat{f}_l$ and $\hat{F}_L$, as detailed in Appendix B.

Substituting Eq. (20) and Eq. (32) into the FPRS collision equation (17) yields the following spectrum equation:

$$\frac{\partial}{\partial t} f_l(\hat{v}, t) = \mathfrak{C}_l(\hat{v}, t), \quad 0 \le l \le l_M, \tag{35}$$

where

$$f_l(\hat{v}, t) = \frac{n_a}{v_{ath}^3} \hat{f}_l(\hat{v}, t), \tag{36}$$

$$\mathfrak{C}_l(\hat{v}, t) = \frac{n_a}{v_{ath}^3} \hat{\mathfrak{C}}_l(\hat{v}, t). \tag{37}$$

Referring to above equation as the 0D-2V FPRS collision spectral equation.

9

3.1.4 Moment constraints

The $(j, l)^{th}$-order normalized kinetic moment of species a, denoted as $\hat{M}_{j,l}$, is generally defined as:

$$\hat{M}_{j,l}(t) = \hat{M}_j\left[\hat{f}_l\right] = 4\pi \int_0^\infty (\hat{v})^{j+2}\hat{f}_l(\hat{v}, t)\,\mathrm{d}\hat{v}. \tag{38}$$

The first few orders of $\hat{M}_{j,l}$ specifically relative to the conserved moments satisfy the following relations:

$$\hat{n}_a(t) = \hat{M}_{0,0}, \tag{39}$$

$$\hat{I}_a(t) = \frac{I_a}{\rho_a v_{ath}} = \frac{1}{3}\hat{M}_{1,1}, \tag{40}$$

$$\hat{K}_a(t) = \frac{K_a}{n_a T_a} = \hat{M}_{2,0}. \tag{41}$$

Theoretically, $\hat{n}_a(t)$ is conserved and equal to 1. The momentum is defined as $I_a(t) = \rho_a(\mathbf{u}_a \cdot \mathbf{e}_z)$ where the average velocity $\mathbf{u}_a(t) = n_a^{-1}\int \mathbf{v}f(\mathbf{v}, t)\,\mathrm{d}\mathbf{v}$, temperature $T_a(t) = m_a v_{ath}^2/2$ and total energy $K_a(t) = \frac{m_a}{2}\int \mathbf{v}^2 f(\mathbf{v}, t)\,\mathrm{d}\mathbf{v}$. The normalized average velocity $\hat{u}_a(t) = (\mathbf{u}_a \cdot \mathbf{e}_z)/v_{ath}$, which is equivalent to $\hat{I}_a$. Similar to the normalized kinetic moment (38), we define the $(j, l)^{th}$-order normalized kinetic dissipative force of species a as follows:

$$\hat{\mathcal{R}}_{j,l}(t) = \hat{\mathcal{R}}_j\left[\hat{\mathfrak{C}}_l\right] = 4\pi \int_0^\infty (\hat{v})^{j+2}\hat{\mathfrak{C}}_l(\hat{v}, t)\,\mathrm{d}\hat{v}. \tag{42}$$

Multiplying both sides of the FPRS collision spectral equation (35) by $4\pi m_a v^{j+2}\mathrm{d}v$ and integrating over the semi-infinite interval $v = [0, \infty)$, simplifying the result gives the $(j, l)^{th}$-order FPRS collision spectral equation in weak form:

$$\frac{\partial}{\partial t}\left[4\pi \rho_a(v_{ath})^j \int_0^\infty (\hat{v})^{j+2}\hat{f}_l(\hat{v}, t)\mathrm{d}\hat{v}\right] = 4\pi \rho_a(v_{ath})^j \int_0^\infty (\hat{v})^{j+2}\hat{\mathfrak{C}}_l(\hat{v}, t)\mathrm{d}\hat{v}, \tag{43}$$

where the mass density $\rho_a = m_a n_a$. In particular, applying Eqs. (38)-(42), we can derive the following relations from the weak form of the FPRS collision spectrum equation (43), reads:

$$\delta_t \hat{n}_a(t) := \frac{\partial_t n_a}{n_a} = \hat{\mathcal{R}}_{0,0}, \tag{44}$$

$$\delta_t \hat{I}_a(t) := \frac{\partial_t I_a}{\rho_a v_{ath}} = \frac{1}{3}\hat{\mathcal{R}}_{1,1}, \tag{45}$$

$$\delta_t \hat{K}_a(t) := \frac{\partial_t K_a}{n_a T_a} = \frac{3}{2}\hat{\mathcal{R}}_{2,0}. \tag{46}$$

Applying Eqs. (44)-(46), one can derive the following relation:

$$\delta_t \hat{T}_a(t) = \delta_t \hat{K}_a\left[2\hat{I}_a\left(\delta_t \hat{I}_a - \hat{I}_a\frac{1}{v_{ath}}\frac{\partial v_{ath}}{\partial t}\right) + \hat{K}_a\frac{1}{v_{ath}}\frac{\partial v_{ath}}{\partial t}\right] \equiv 0. \tag{47}$$

The above equation serves as a convergence criterion for our algorithm in solving the FPRS collision spectral equation (35).

Mass, momentum and energy conservation (5)-(7) can be reformulated as a function

of $\hat{\mathfrak{C}}_{lab}$ (give in Eq. (34)), reads:

$$\left\langle 1, \hat{\mathfrak{C}}_{0ab} \right\rangle_{\hat{v}} = \left\langle 1, \hat{\mathfrak{C}}_{0ba} \right\rangle_{\hat{v}_b} = 0, \tag{48}$$

$$\rho_a v_{ath} \left\langle \hat{v}, \hat{\mathfrak{C}}_{1ab} \right\rangle_{\hat{v}} = -\rho_b v_{bth} \left\langle \hat{v}_b, \hat{\mathfrak{C}}_{1ba} \right\rangle_{\hat{v}_b}, \tag{49}$$

$$\frac{\rho_a \left(v_{ath}\right)^2}{2} \left\langle (\hat{v})^2, \hat{\mathfrak{C}}_{0ab} \right\rangle_{\hat{v}} = -\frac{\rho_b \left(v_{bth}\right)^2}{2} \left\langle (\hat{v}_b)^2, \hat{\mathfrak{C}}_{0ba} \right\rangle_{\hat{v}_b}, \tag{50}$$

where $\left\langle (\hat{v})^j, g \right\rangle_{\hat{v}}$ denotes the integral of $4\pi(\hat{v})^{j+2} \cdot g$ with respect to $\hat{v}$. These conservation constraints are activated when enforcing discrete conservation (details provided in Sec. 4.2) of the normalized FPRS collision operator (give in Eq. (14)). Otherwise, they serve as indicators to evaluate the performance of our algorithm.

3.2 Speed coordinate

By selecting sufficient large values of l_M and L_M, the spectral equation (35) can closely approximate the original FPRS collision equation (17) with high accuracy. However, due to the time-discrete error and velocity-discrete errors, it is not feasible to directly obtain the proper distribution function for general scenarios which are typically nonlinear multi-scale systems. Nevertheless, phenomena that are more closely related to the conserved moments in both l space and j space, are usually crucial for system evolution and of greater interest to physicists. Therefore, an algorithm that approximates the distribution function based on the convergence of kinetic moments with a specific collection of (j, l) - including mass, momentum and total energy conservation - will be preferred.

Moreover, in the SHE together with KFE framework, the smoothness of $f(v, \mu, t)$ leading to continuous differentiability of all amplitudes, $\hat{f}_l(\hat{v}, t)$. Additionally, continuity in system evolution over time is also assumed. In contrast to the previous work utilizing the multi-quadric radial basis function[31], a new function named King (details in Appendix A) is introduced in speed coordinate. Based on the King function, King method is developed as a moment convergence technology for approximating the desired functions.

3.2.1 King method

The new King function, which is associated with the first class of modified Bessel functions, can be defined as following:

$$\mathcal{K}_l(\hat{v}; \iota, \sigma) = \frac{(l + 1/2)}{\sigma^2 \sqrt{2|\iota| \hat{v}}} \left(\frac{|\iota|}{\iota}\right)^l e^{-\sigma^{-2}(\hat{v}^2 + \iota^2)} \mathrm{Besseli}\left(\frac{2l+1}{2}, 2\frac{|\iota|}{\sigma^2}\hat{v}\right). \tag{51}$$

In this context, the independent variable $\hat{v} \in [0, \mathbb{R}^+]$ and the parameter $l \in [0, \mathbb{N}^+]$, representing the order of the King function. The parameters ι and σ are characteristic parameters of the King function, satisfying $\sigma \in \mathbb{R}^+$ and $\iota \in \mathbb{R}$.

The lth-order King function, $\mathcal{K}_l(\hat{v}; \hat{u}_a, \hat{v}_{ath})$ (give in Eq. (51)) has the same asymptotic behaviour (details in Appendix A) as the lth-order amplitude of the normalized distribution function, $\hat{f}_l(\hat{v}, t)$ (give in Eq. (22)). Therefore, we can effectively approximate $\hat{f}_l(\hat{v}, t)$ using the King function as follows:

$$\hat{f}_l(\hat{v}, t) = \frac{2\pi}{\pi^{3/2}} \sum_{s=1}^{N_{Ka}} [\hat{n}_{a_s} \mathcal{K}_l(\hat{v}; \hat{u}_{a_s}, \hat{v}_{ath_s})]. \tag{52}$$

Name $\hat{u}_{a_s}$ as the characteristic group velocity. The number of King function, $N_{K_a} \in \mathbb{N}^+$ is a predetermined value at the initial time level but determined by the subsequent optimization scheme (details in Sec. 3.2.2). Referring Eq. (52) as the King function expansion (KFE), which is a parameter model for the amplitude function. The theoretical convergence of KFE can be established by utilizing Wiener's Tauberian theorem[56], and a heuristic proof is provided in a subsequent work[49] posted on arXiv.

Multiplying both sides of Eq. (52) by $4\pi\hat{v}^{j+2}\mathrm{d}\hat{v}$ and integrating over the semi-infinite interval $\hat{v} = [0,\infty)$ yields the following characteristic parameter equations (CPEs):

$$\hat{\mathcal{M}}_{j,l}(t) = \begin{cases} C_{M^l_j} \sum_{s=1}^{N_{K_a}} \hat{n}_{a_s}(\hat{v}_{ath_s})^j \left(\dfrac{\hat{u}_{a_s}}{\hat{v}_{ath_s}}\right)^l \left[1 + \sum_{\gamma=1}^{j/2} C^\gamma_{j,l} \left(\dfrac{\hat{u}_{a_s}}{\hat{v}_{ath_s}}\right)^{2\gamma}\right], & l \in 2\mathbb{N}, \\[4mm] C_{M^l_j} \sum_{s=1}^{N_{K_a}} \hat{n}_{a_s}(\hat{v}_{ath_s})^j \left(\dfrac{\hat{u}_{a_s}}{\hat{v}_{ath_s}}\right)^l \left[1 + \sum_{\gamma=1}^{(j-1)/2} C^\gamma_{j,l} \left(\dfrac{\hat{u}_{a_s}}{\hat{v}_{ath_s}}\right)^{2\gamma}\right], & l \in 2\mathbb{N}+1, \end{cases} \tag{53}$$

where $j \in \{(l+2j_p-2)|j_p \in \mathbb{N}^+\}$. The coefficients $C^\gamma_{j,l}$ and $C_{M^l_j}$ are given by:

$$C^\gamma_{j,l} = 2^\gamma \frac{(2l+1)!! C_\gamma^{(j-l)/2}}{(2l+2\gamma+1)!!}, \quad C_{M^l_j} = \frac{1}{2^{(j-l)/2}} \frac{(l+j+1)!!}{(2l-1)!!}. \tag{54}$$

Symbol $C_\gamma^{(j-l)/2}$ denotes the binomial coefficient. In particular, when all $\hat{u}_{a_s}$ are zero, the CPEs will be reduced to:

$$\hat{\mathcal{M}}_{j,l}(t) = C_{M^l_j} \sum_{s=1}^{N_{K_a}} \hat{n}_{a_s}(\hat{v}_{ath_s})^j, \quad l \in 2\mathbb{N}. \tag{55}$$

Note that the original definition of normalized kinetic moment (38), $\hat{M}_{j,l}$, represents the numerical value calculated from the amplitude function before being smoothed by King function in this research. This is accomplished through the utilization of a Romberg integral[46] given by Eq. (69). While $\hat{\mathcal{M}}_{j,l}$ denotes the desired form in physics derived from the KFE model (52). The relative optimization error is defined as:

$$\delta\hat{\mathcal{M}}_{j,l}(t) = \left|\hat{M}_{j,l} - \hat{\mathcal{M}}_{j,l}\right| / \left|\hat{M}_{j,l}\right|, \tag{56}$$

which will be utilized to assess the convergence of the optimization process.

Due to the rapid damping of the higher-order harmonics, the first few harmonics in SHE (20) contain much of the most important physics for many plasma physical problems of interest. Therefore, we can assume that the characteristic parameters $\hat{n}_{a_s}$, $\hat{u}_{a_s}$ and $\hat{v}_{ath_s}$ in KFE (52) are independent of l. This assumption allows us to approximate the normalized function $\hat{f}(\hat{v},\mu,t)$ by N_{K_a} Gaussian functions, $\hat{f}(\hat{v},\mu,t) = \sum_{s=1}^{N_{K_a}} \frac{1}{\pi^{3/2}} \frac{\hat{n}_{a_s}}{\hat{v}_{ath_s}^3} e^{-(\hat{v}-\hat{u}_{a_s}\mathbf{e}_z)^2}$. This approximation is reasonable and efficient, particularly for weakly anisotropic plasmas in which each sub-component $\mathcal{K}_l$ is not far from a local equilibrium state (the characteristic group velocity, $|\hat{u}_{a_s}| \ll 1$). Therefore, the distribution function is characterized by a total of $3N_{K_a}$ unknown parameters. Given knowledge of any specified $3N_{k_a}$ kinetic moments $\hat{\mathcal{M}}_{j,l}$ with a collection of (j,l), then solving the corresponding well-posed CPEs (53) can provide us with all the characteristic parameters. For weakly anisotropic plasmas, the following section provides three specific optimization schemes, L01jd2nh, L01jd2 and L01jd2NK, all of which are convergent for higher-order moments.

3.2.2 Optimization scheme for characteristic parameters

In l space, it is preferable to choose the kinetic moments of the first two orders amplitude functions for weakly anisotropic plasmas, due to the simplicity of the corresponding CPEs (53). Following the principle of simplicity, we propose the following optimization scheme by selecting the collection of kinetic moments in j space,

$$(j, l) \in \{(2j_p + l, l) | j_p \in \mathbb{N}, 0 \leq l \leq 1, 0 \leq 2j_p + l < 3N_{K_a}\} . \tag{57}$$

This will be referred as the **L01jd2nh** scheme. In particular, when $(j, l) = (1, 1)$, CPEs represented by Eq. (53) yields:

$$\sum\nolimits_{s=1}^{N_{K_a}} \hat{n}_{a_s} \hat{u}_{a_s} = \hat{\mathcal{M}}_{1,1}/3 = \hat{u}_a . \tag{58}$$

When $(j, l) = (0, 0)$ and $(j, l) = (2, 0)$, CPEs gives:

$$\sum\nolimits_{s=1}^{N_{K_a}} \hat{n}_{a_s} = \hat{\mathcal{M}}_{0,0} = \hat{n}_a, \tag{59}$$

$$\sum\nolimits_{s=1}^{N_{K_a}} \hat{n}_{a_s} \left[3(\hat{v}_{ath_s})^2/2 + (\hat{u}_{a_s})^2 \right] = \hat{\mathcal{M}}_{2,0} = 3/2 + (\hat{u}_a)^2 . \tag{60}$$

Eqs. (58)-(60) serve as conservation constraints and will be utilized as the constraint equations for L01jd2nh, as well as the subsequent L01jd2 scheme. This indicates that when $N_{K_a} \geq 1$, the L01jd2nh scheme can ensure conservation of mass, momentum and energy during the optimization process.

When the parameters $\hat{n}_{a_s}$ of species a are all nearly constant, a more effective scheme named **L01jd2**, rather than L01jd2nh, can be utilized. Here, assuming that $\hat{n}_{a_s}$ are constants and any $2N_{K_a}$ normalized kinetic moments, $\hat{\mathcal{M}}_{j,l}$ could be employed in CPEs (53) to determine the parameters $\hat{u}_{a_s}$ and $\hat{v}_{ath_s}$. In the L01jd2 scheme, N_{K_a} will remain constant and

$$(j, l) \in \left\{(2j_p - l, l) | j_p \in \mathbb{N}^+, 0 \leq l \leq 1, 1 \leq j_p < N_{K_a}\right\} . \tag{61}$$

The **L01jd2NK** scheme is obtained by integrating the L01jd2nh scheme and the L01jd2 scheme, using the criterion given by:

$$\delta \hat{n}_{a_s} = |\hat{n}_{a_s}(t_{k+1}) - \hat{n}_{a_s}(t_k)| / \hat{n}_{a_s}(t_k), \quad s = 1, 2, \cdots, N_{K_a}, \tag{62}$$

where the superscripts, k and $k + 1$, denote the time levels. When the characteristic parameters of species a satisfy $(N_{K_a})^{-1} \sum_{s=1}^{N_{K_a}} \delta \hat{n}_{a_s} \leq rtol_n$, where $rtol_n$ is a specified relative tolerance, the L01jd2 scheme will be executed. Otherwise, the L01jd2nh scheme will be performed within L01jd2NK scheme. Unless otherwise stated, the parameter $rtol_n = 0.1$.

Especially, when all parameters $\hat{u}_{a_s}$ are zero, the L01jd2nh scheme simplifies to:

$$(j, l) \in \left\{(2j_p - 2, l) | j_p \in \mathbb{N}^+, 1 \leq j_p \leq 2N_{K_a}, l = 0\right\} \tag{63}$$

and the L01jd2 scheme becomes:

$$(j, l) \in \left\{(2j_p, l) | j_p \in \mathbb{N}^+, 1 \leq j_p \leq N_{K_a}, l = 0\right\} . \tag{64}$$

Meanwhile, the conservation constraints represented by Eqs. (58)-(60) are reduced to:

$$\hat{\mathcal{M}}_{1,1} = 0, \quad \hat{\mathcal{M}}_{0,0} = 2\hat{\mathcal{M}}_{2,0}/3 = 1 . \tag{65}$$

Eq. (63) and Eq. (64) show that if N_{K_a} increases by one, the convergence order j increases by two in the L01jd2 scheme and by four in the L01jd2nh scheme when $N_{K_a} \geq 2$.

After specifying the optimization scheme with a collection of (j, l) and computing the normalized kinetic moments $\hat{M}_{j,l}$, we can approximate $\hat{\mathcal{M}}_{j,l}$ by let $\hat{\mathcal{M}}_{j,l} = \hat{M}_{j,l}$. Hence, the parameters $\hat{n}_{a_s}$, $\hat{u}_{a_s}$ and $\hat{v}_{ath_s}$ can be solved from the well-posed CPEs (53) by utilizing a least squares method[57] (LSM), specifically Levenberg-Marquardt[58,59] method. The main procedure for the King method is outlined in Algorithm 1. In order to enclose the non-linear FPRS collision spectral equation (35), the approximation of $\hat{f}_l$ when $l \geq 2$ can be achieved through the utilization of KFE (52) with established characteristic parameters. The remaining question is how to determine the number of King functions, N_{K_a}, at a new time level. This will be provided in the following section.

Algorithm 1 Employing King method to smooth the normalized amplitude functions of species a

---

From inputs $l_M(t)$, $N_{K_a}(t)$, $\hat{v}_\alpha(t)$, collection of (j, l) and $\hat{f}_l(\hat{v}_\alpha(t), t)$

    1 Compute the normalized kinetic moments $\hat{M}_{j,l}(t)$ (92)

    2 Let $\hat{\mathcal{M}}_{j,l} := \hat{M}_{j,l}(t)$ update $\hat{n}_{a_s}(t)$, $\hat{u}_{a_s}(t)$, $\hat{v}_{ath_s}(t)$ by solving CPEs (91)

    3 Evaluate the new number of King functions, $N_{K_a}(t^*)$ according to algorithm 2

  If $N_{K_a}(t^*) \neq N_{K_a}(t)$

        4 Let $N_{K_a}(t) := N_{K_a}(t^*)$

        5 Update the collection of (j, l) based on $N_{K_a}(t^*)$

        6 Solve the CPEs (91) again

  End

    7 Evaluate the convergence of optimization by calculate $\delta\hat{\mathcal{M}}_{j,l}$ according to Eq. (56)

    8 Update $l_M(t)$ and the smoothed amplitudes, $\hat{f}_l(\hat{v}_\alpha(t), t)$ according to Eq. (90)

    9 **Return** $l_M(t)$, $N_{K_a}(t)$, $\hat{v}_\alpha(t)$, collection of (j, l) and $\hat{f}_l(\hat{v}_\alpha(t), t)$

3.2.3 Update N_{K_a}

The adaptability of N_{K_a} is essential for capturing the nonlinear effects of plasma systems. Before providing the self-adaptive scheme for N_{K_a}, we introduce an indistinguishable condition represented by Eq. (66) for KFE (52). If two known groups of characteristic parameters (ι_1, σ_1) and (ι_2, σ_2) in KFE, each with respective weights $\hat{n}_{a_1}$ and $\hat{n}_{a_2}$, satisfy

$$\left| \frac{\sigma_1}{\sigma_2} - 1 \right| + \left| \frac{\iota_1}{\iota_2} - 1 \right| \leq rtol, \tag{66}$$

we claim that the King function $\mathcal{K}_l(\hat{v}; \iota_1, \sigma_1)$ and $\mathcal{K}_l(\hat{v}; \iota_2, \sigma_2)$ are identical with parameters (ι_0, σ_0), within the allowed error range. Here, $rtol$ is a specified relative tolerance with a default value of $rtol = 10^{-10}$. The weight of $\mathcal{K}_l(\hat{v}; \iota_0, \sigma_0)$ is determined by $\hat{n}_{a_0} = \hat{n}_{a_1} + \hat{n}_{a_2}$.

The number of King functions at the $(k+1)^{th}$ time level will be determined by the given scheme until reaching a specified minimum value, N_K^{min}, or maximum value, N_K^{max}. For weakly anisotropic plasmas, a effective scheme to update N_{K_a} is provided as follows:

$$N_{K_a}(t_{k+1}) = N_{K_a}(t_k) - dN_{K_a}(t_k), \tag{67}$$

where

$$dN_{K_a}(t_k) = \begin{cases} 0, & Eq. \ (66) == false, \\ 1, & Eq. \ (66) == true \ . \end{cases} \tag{68}$$

The value of N_{K_a} at the first time level is set to a specified constant, N_K, where $N_K^{min} \leq N_K \leq N_K^{max}$. The values of $N_K^{min} = 1$ and $N_K^{max} = 3$ have been achieved at present.

When $N_{K_a}(t_{k+1}) < N_{K_a}(t_k)$, we can eliminate the higher-order CPEs, which are usually more complex, to obtain an updated well-posed CPEs. The procedures for determining $N_{K_a}(t_{k+1})$ is outlined in Algorithm 2. However, it should be noted that the method for updating N_{K_a} is not limited to the aforementioned method. A more advanced technique, capable of self-adaptive increase in N_{K_a} with the potential for N_K^{max} to reach up to 10, is presented in our subsequent work[49] and will be further refined in our future research.

Algorithm 2 Determine parameter N_{K_a} at the $(k+1)^{th}$ time level.

If optimization scheme == L01jd2

    $N_{K_a}(t_{k+1}) \equiv N_{K_a}(t_0)$

Else

    If $k = 0$

        $N_{K_a}(t_{k+1}) = N_K$

    Else

        If Eq. (66) == **True** $dN_{K_a}(t_k) = 1$ **Else** $dN_{K_a}(t_k) = 0$ **End**

        $N_{K_a}(t_{k+1}) = \min\{N_K^{max}, \max[N_K^{min}, N_{K_a}(t_k) - dN_{K_a}(t_k)]\}$

    End

End

3.2.4 Discretization of speed coordinate

In order to calculate the normalized kinetic moments $\hat{M}_{j,l}$ (38) and the Shkarofsky's integrals (give in Eqs. (30)-(31)), a set of field nodes in speed coordinate is required. In this research, we employ uniform field nodes in a normalized speed domain of $[0, \hat{v}_M]$, where $\hat{v}_M$ denotes the maximum value of the normalized speed. If not specified otherwise, $\hat{v}_M$ is a constant with a default value of 10. The total number of the field nodes, $N_n = 2^{n_2} + 1$ where $n_2 \in \mathbb{N}^+$. Let $\hat{v}_\alpha$ represent the αth field node and $[\hat{v}_\alpha]$ denote the field nodes set where $\alpha = 1, 2, \cdots, N_n$. The spacing, $\Delta\hat{v}_\alpha$, is then determined as $\Delta\hat{v}_\alpha = \hat{v}_M/2^{n_2}$. The default value for parameter n_2 are set at $n_2 = 7$, unless otherwise stated. Therefore, the default number of nodes, N_n will be 129.

The normalized kinetic moments $\hat{M}_{j,l}$ (38) will be calculated using the Romberg integral[46] method. For convenience, the value and its relative error will be expressed as:

$$\hat{M}_{j,l}(t), Error\left(\hat{M}_{j,l}\right) = \left\langle ([\hat{v}_\alpha])^j | \hat{f}_l([\hat{v}_\alpha], t) \right\rangle_R, \tag{69}$$

denoting the Romberg integral of function $(\hat{v})^{j+2}\hat{f}_l(\hat{v})$ over the set $[\hat{v}_\alpha]$. Symbol $Error\left(\hat{M}_{j,l}\right)$ represents the estimated upper bound of the integral error of $\hat{M}_{j,l}$. The set $[\hat{v}_\alpha]$ represents the uniform nodes (depicted as red points in Fig. 3). Similarly, the computation of Eq. (42) will also be performed using Romberg integral:

$$\hat{\mathcal{R}}_{j,l}(t), Error\left(\hat{\mathcal{R}}_{j,l}\right) = \left\langle ([\hat{v}_\alpha])^j | \hat{\mathfrak{C}}_l([\hat{v}_\alpha], t) \right\rangle_R. \tag{70}$$

The relative errors, $Error\left(\hat{M}_{j,l}\right)$ and $Error\left(\hat{\mathcal{R}}_{j,l}\right)$ can serve as indicators to evaluate the

quality of field nodes determined by parameters (n_2, N_0). These indicators could be utilized in constructing a self-adaptive scheme which will be developed in the future.
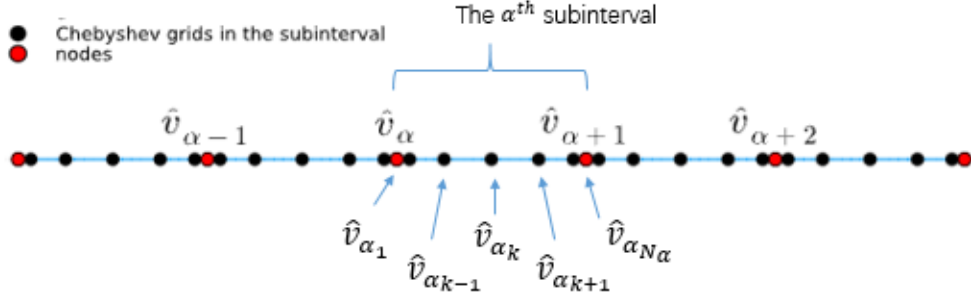

Figure 3: Discretization of speed coordinate: field nodes and the Chebyshev grids in the subinterval.

Similar to Eq. (52), the lth-order normalized amplitude function of the background species b, $\hat{F}_L(\hat{v}_b, t)$, can be approximated as:

$$\hat{F}_L(\hat{v}_b, t) = \frac{2\pi}{\pi^{3/2}} \sum_{r=1}^{N_{K_b}} [\hat{n}_{b_r} \mathcal{K}_L(\hat{v}; \hat{u}_{b_r}, \hat{v}_{bth_r})] . \tag{71}$$

The number of King functions for species b, $N_{K_b} \in \mathbb{N}^+$, may not be equivalent to the one of species a, N_{K_a}. The Shkarofsky's integrals, given in Eqs. (30)-(31), involve variable upper/lower bound integration and remain challenging to compute analytically. In this study, they are numerically evaluated using a set of refined grids, as illustrated in Fig. 3.

To create the αth subinterval $[\hat{v}_{\alpha k}], k = 1, 2, \cdots, N_\alpha$, we add $N_\alpha - 2$ auxiliary grids (black points) into the αth interval $[\hat{v}_\alpha, \hat{v}_{\alpha+1}]$, as showed in Fig. 3. For background species b, let $z_{\alpha_k} = v_{abth} \hat{v}_{\alpha_k}$ where $z = \hat{v}_{ab}$ and thermal velocity ratio $v_{abth} = v_{ath}/v_{bth}$. The Shkarofsky's integrals can be calculated using parallel Clenshaw-Curtis (CC) quadrature, which is a type of Gauss-Chebyshev quadrature[34] . This method can be represented as follows:

$$I_{j,L}(z_\alpha, t) = \begin{cases} 0, & \alpha = 1, \\ \frac{1}{(z_\alpha)^j} \sum_{s=2}^{\alpha} \left\langle ([z_{s_k}])^j | \hat{F}_L([z_{s_k}], t) \right\rangle_{CC}, & 2 \le \alpha \le 2^{n_2} + 1, \end{cases} \tag{72}$$

$$J_{j,L}(z_\alpha, t) = \begin{cases} 0, & \alpha = 2^{n_2} + 1, \\ (z_\alpha)^j \sum_{s=\alpha}^{2^{n_2}} \left\langle ([z_{s_k}])^{-j} | \hat{F}_L([z_{s_k}], t) \right\rangle_{CC}, & 1 \le \alpha \le 2^{n_2} . \end{cases} \tag{73}$$

Here, the Clenshaw-Curtis quadrature on the αth subinterval can be formulated as:

$$\left\langle ([z_{\alpha_k}])^j | g([z_{\alpha_k}]) \right\rangle_{CC} = \sum_{k=1}^{N_\alpha} w_k (z_{\alpha_k})^{j+2} g(z_{\alpha_k}) . \tag{74}$$

The set $[z_{\alpha_k}]$ are the Gauss collection on the αth quadrature domain where $k = 1, 2, \cdots, N_\alpha$, while z_{α_k} denotes the kth point on the αth subinterval showed in Fig. 3. The corresponding integral weight w_k is calculated according to Fornberg's algorithm[55] . Function $\hat{F}_L(\hat{v}_{ab}, t)$ denotes the normalized background distribution function of species a. This function can be easily obtained by mapping the analytical function, $\hat{F}_L(\hat{v}_b, t)$ given by Eq. (71), onto the normalized speed coordinate $\hat{v}_{ab}$. This process of mapping can be expressed as:

$$\hat{F}_L(\hat{v}_{ab}, t) = \hat{F}_L(v_{abth} \hat{v}, t) . \tag{75}$$

In this paper, the number of auxiliary Chebyshev grids in subintervals, N_α, is fixed at a given constant N_0 and the auxiliary grids (depicted as black points in Fig. 3) are only utilized in the step for calculating the Shkarofsky's integrals. Consequently, the maximum number of grids in speed coordinate is determined by $N_v = (N_0 - 1)(N_n - 2) + N_0$ and $N_{v2} = l_{M_1} \times N_v$ for the total velocity space. Given the default value of $N_0 = 7$ unless otherwise specified, we obtain $N_v = 769$. It should be noted that N_v and N_{v2} are primarily utilized in the Rosenbluth potentials step (Sec. 3.1.2), while the maximum number of nodes for other steps is determined by number of field nodes, N_n.

It is particularly noteworthy that for moderately anisotropic plasma systems in which some characteristic group velocity $|\hat{u}_{a_s}|$ near one, including the so-called subsonic and low supersonic regions, the characteristic parameters in KFE (52) typically are dependent on l. The framework of SHE together with KFE remains suitable for these general scenarios. However, the optimization scheme need to be extended as a self-adaptive version, incorporating a comprehensive collection of (j, l), a clearer scheme for updating N_{K_a} and self-adaptive field nodes determined by parameters (n_2, N_0). This is beyond the scope of this paper and will be addressed in future research. Additionally , it is worth mentioning that the KFE serves as a smoothing step, combined with the implicit time discretization given in Sec. 4, enabling our algorithm to surpass the classical CFL condition limit. From now on, the subscript and superscript "k" will represent the time level.

4 Implicit temporal discretization and nonlinear conservation constraints

Given the specified discretization of speed coordinate determined by the value of $\hat{v}_M$ and parameters (n_2, N_0), the semi-discrete FPRS collision spectrum equations (35) at the αth node can be formulated as:

$$\frac{\partial}{\partial t} f_l(\hat{v}_\alpha, t) = \mathfrak{C}_l(\hat{v}_\alpha, t), \quad 0 \le l \le l_M . \tag{76}$$

where

$$f_l(\hat{v}_\alpha, t) = \frac{n_a}{v_{ath}^3} \hat{f}_l(\hat{v}_\alpha, t), \tag{77}$$

$$\mathfrak{C}_l(\hat{v}_\alpha, t) = \frac{n_a}{v_{ath}^3} \sum_{b=1}^{N_s} \frac{n_b}{v_{bth}^3} \Gamma_{ab} \hat{\mathfrak{C}}_{lab}, \tag{78}$$

$$\hat{\mathfrak{C}}_{lab}(\hat{v}_\alpha, t) = \sum_{\beta=1}^{l_{M_1}} w_{\mu_\beta} P_l(\mu_\beta) \hat{\mathfrak{C}}_{ab}(\hat{v}_\alpha, \mu_\beta, t) . \tag{79}$$

Here, function $\hat{\mathfrak{C}}_{ab}$ is a nonlinear function of $\hat{f}_l$ and $\hat{F}_L$ and satisfies the form presented in Appendix B. Number density remains constant theoretically and thermal velocity, v_{ath}, is a function of ρ_a, I_a (40) and K_a (41), reads:

$$v_{ath} = \sqrt{\frac{2}{3}\left(\frac{2K_a}{\rho_a} - \left(\frac{I_a}{\rho_a}\right)^2\right)} . \tag{80}$$

The final semi-discrete scheme for the nonlinear FPRS collision equations is derived by incorporating the aforementioned equations, including the FPRS collision spectrum equations (76), the FPRS collision operators represented by Eqs. (78)-(79) and (137). The King function expansion (52) acts as a smoothing step, while the characteristic parameter equations (53), convergence criterion (47) and conservation equations (48)-(50) serve as constraints for FPRS collision spectrum equations (76).

4.1 Implicit temporal discretization

4.1.1 Time block technique

The discrete form of FPRS collision spectrum equation (76) utilizing explicit Euler scheme[45] can be formulated as follows:

$$f_l\left(\hat{v}_\alpha^k, t_{k+1}\right) \;=\; f_l\left(\hat{v}_\alpha^k, t_k\right) + \Delta_{t_k}\mathfrak{C}_l\left(\hat{v}_\alpha^k, t_k\right), \tag{81}$$

where $\Delta t_k = t_{k+1} - t_k$ represents the current timestep size. Similarly,

$$X_a\left(t_{k+1}\right) \;=\; X_a\left(t_k\right) + \Delta_{t_k}\partial_t X_a\left(t_k\right), \quad X = n, I, K. \tag{82}$$

After computing v_{ath}^{k+1} (80) and $\hat{f}_l\left(\hat{v}_\alpha^k, t_{k+1}\right)$ (77), applying the King method provided by Algorithm 1 yields the analytical formula of $f_l\left(\hat{v}_\alpha^k, t_{k+1}\right)$. Notes that $f_l\left(\hat{v}_\alpha^k, t_{k+1}\right)$ in Eq. (81) is evaluated on the normalized speed coordinate at the kth time level, $\hat{v}_\alpha^k = v_\alpha^k/v_{ath}^k$.

Regard the interval $[t_k, t_{k+1}]$ as the kth time block. The time block technique (TBT) suggests that within the kth time block, $v_\alpha(t)$ remains invariant and will be updated at the $(k+1)^{th}$ time level within the $(k+1)^{th}$ time block. The default update will keep $\hat{v}_\alpha^{k+1}$ equivalent to $\hat{v}_\alpha^k$, determined by $\hat{v}_M$ and (n_2, N_0). Defining $\hat{v}_\alpha^{k,k+1} = v_\alpha^k/v_{ath}^{k+1}$ gives

$$\hat{v}_\alpha^{k,k+1} \;=\; \hat{v}_\alpha^k v_{ath}^k/v_{ath}^{k+1}, \tag{83}$$

Hence, the amplitude function on α^{th} node at $(k+1)^{th}$ time level within k^{th} time block is:

$$f_l\left(\hat{v}_\alpha^{k,k+1}, t_{k+1}\right) \;=\; f_l\left(\hat{v}_\alpha^k v_{ath}^k/v_{ath}^{k+1}, t_{k+1}\right). \tag{84}$$

The successful application of TBT relies on the analytical KFE (52) in King method.

The explicit Euler scheme is a first-order precision algorithm, which can be employed as the prediction step (first stage) of an implicit algorithm, such as the trapezoidal scheme. Moreover, TBT is also effective in Trapezoidal scheme, presented in Algorithm 7. The main procedure for solving FPRS collision spectrum equation within k^{th} time block utilizing the explicit Euler scheme is outlined in the following pseudo-code (Algorithm 3).

Algorithm 3 Solving FPRS collision spectrum equation by utilizing explicit Euler scheme

From inputs Δ_{t_k}, $l_M(t_k)$, $N_{K_a}(t_k)$, $\hat{v}_\alpha^k$, collection of (j, l) and $f_l(\hat{v}_\alpha^k, t_k)$ for all species
  1 Calculate $\frac{\partial}{\partial t}n_a^k$, $\frac{\partial}{\partial t}I_a^k$, $\frac{\partial}{\partial t}K_a^k$, $\hat{v}_\alpha^k$ and $\mathfrak{C}_l(\hat{v}_\alpha^k, t_k)$ according to Algorithm 5
  2 Evaluate $f_l(\hat{v}_\alpha^k, t_{k+1})$ according to Eq. (81)
  3 Calculate n_a^{k+1}, I_a^{k+1}, K_a^{k+1} according to Eq. (82)
  4 Update v_{ath}^{k+1} according to Eq. (80) and $\hat{f}_l(\hat{v}_\alpha^k, t_{k+1})$ according to Eq. (77)
  5 Smooth $\hat{f}_l(\hat{v}_\alpha^k, t_{k+1})$ utilizing King method presented by Algorithm 1
  6 Update $\hat{v}_\alpha^{k,k+1}$ according to Eq. (83) and $f_l(\hat{v}_\alpha^{k,k+1}, t_{k+1})$ according to Eq. (84)
  7 **Return** $\frac{\partial}{\partial t}n_a^k$, $\frac{\partial}{\partial t}I_a^k$, $\frac{\partial}{\partial t}K_a^k$, $\mathfrak{C}_l(\hat{v}_\alpha^k, t_k)$, v_{ath}^{k+1}, $\hat{v}_\alpha^{k,k+1}$ and $f_l(\hat{v}_\alpha^{k,k+1}, t_{k+1})$

4.1.2 Implicit iteration

For equation $\partial_t A = g(A)$, the discretization employing trapezoidal[45] scheme can be formulated as follows:

$$A^{k+1} \;=\; A^k + \Delta_{t_k}\left[c_k g\left(A^k\right) + c_{k+1} g\left(A^{k+1*}\right)\right], \tag{85}$$

where the coefficients c_k and c_{k+1} represent the temporal weights for Range-Kutta method. In the trapezoidal scheme, both of them are equal to $1/2$. During the implicit iteration to optimize the convergence of A at $(k+1)^{th}$ time level, A^{k+1} denotes the value of A at the ith stage of $(k+1)^{th}$ time level, while A^{k+1*} represents the value of A at the $(i-1)^{th}$ stage of $(k+1)^{th}$ time level, where $i = 2, 3, \cdots, N_{in}$. The maximum number of implicit iteration within each time block is denoted as N_{in}, typically set to a default value of 10.

By employing the trapezoidal scheme for time integration, the discrete FPRS collision spectral equation (76) at α^{th} node and within k^{th} time block can be formulated as:

$$f_l\left(\hat{v}_\alpha^{k,k+1}, t_{k+1}\right) = f_l\left(\hat{v}_\alpha^k, t_k\right) + \Delta_{t_k}\left[c_k\mathfrak{C}_l\left(\hat{v}_\alpha^k, t_k\right) + c_{k+1}\mathfrak{C}_l\left(\hat{v}_\alpha^{k,k+1}, t_{k+1}\right)\right] . \quad (86)$$

The pseudo-code for solving Eq. (86) is provided by Algorithm 7. The lth-order amplitude of FPRS collision operator at α^{th} node and $(k+1)^{th}$ time level within k^{th} time block are:

$$\mathfrak{C}_l\left(\hat{v}_\alpha^{k,k+1}, t_{k+1}\right) = \frac{n_a^{k+1}}{\left(v_{ath}^{k+1}\right)^3}\sum_{b=1}^{N_s}\frac{n_b^{k+1}}{\left(v_{bth}^{k+1}\right)^3}\Gamma_{ab}^{k+1}\hat{\mathfrak{C}}_{lab}\left(\hat{v}_\alpha^{k,k+1}, t_{k+1}\right), \quad (87)$$

where

$$\hat{\mathfrak{C}}_{lab}\left(\hat{v}_\alpha^{k,k+1}, t_{k+1}\right) = \sum_{\beta=1}^{l_{M_1}}w_{\mu_\beta}^{k+1}P_l(\mu_\beta^{k+1})\hat{\mathfrak{C}}_{ab}\left(\hat{\mathbf{v}}^{k,k+1}, t_{k+1}\right) . \quad (88)$$

Here $\hat{\mathbf{v}}^{k,k+1} = \mathbf{v}^k/v_{ath}^{k+1}$. The normalized FPRS collision operator, $\hat{\mathfrak{C}}_{ab}$, satisfies Eq. (137), which is a nonlinear model and can be rewritten as:

$$\begin{aligned}
\hat{\mathfrak{C}}_{ab}\left(\hat{\mathbf{v}}^{k,k+1}, t_{k+1}\right) = \hat{\mathfrak{C}}_{ab}\Big[&\hat{f}_0\left(\hat{v}_\alpha^{k,k+1}, t_{k+1}\right), \cdots, \hat{f}_l\left(\hat{v}_\alpha^{k,k+1}, t_{k+1}\right), \cdots, \hat{f}_{l_{max}}\left(\hat{v}_\alpha^{k,k+1}, t_{k+1}\right), \\
&\hat{F}_0\left(v_{abth}^{k+1}\hat{v}_\alpha^{k,k+1}, t_{k+1}\right), \cdots, \hat{F}_L\left(v_{abth}^{k+1}\hat{v}_\alpha^{k,k+1}, t_{k+1}\right), \cdots \hat{F}_{l_{max}}\left(v_{abth}^{k+1}\hat{v}_\alpha^{k,k+1}, t_{k+1}\right)\Big] .
\end{aligned} \quad (89)$$

Note that N_{K_a}, N_{K_b}, l_{max} are also recalculated at each time level. The scheme to update N_{K_a} is provided in Sec. 3.2.3. The main procedure for computing normalized FPRS collision operator between species a and species b at $(k+1)^{th}$ time level within k^{th} time block is outlined in Algorithm 4, while procedure for calculating the FPRS collision operator of species a at the $(k+1)^{th}$ time level within k^{th} time block is outlined in Algorithm 5.

Algorithm 4 Calculating the normalized FPRS collision operator between species a and species b at $(k+1)^{th}$ time level within k^{th} time block

---

From inputs n_a^{k+1}, v_{ath}^{k+1}, $l_M(t_{k+1})$, $N_{K_a}(t_{k+1})$, $\hat{v}_\alpha^{k,k+1}$ and $\hat{f}_l(\hat{v}_\alpha^{k,k+1}, t_{k+1})$ for all species
  1 Evaluate $\frac{\partial}{\partial \hat{v}}\hat{f}_l(\hat{v}_\alpha^{k,k+1}, t_{k+1})$, $\frac{\partial^2}{\partial \hat{v}^2}\hat{f}_l(\hat{v}_\alpha^{k,k+1}, t_{k+1})$ according to KFE (90)
  2 Update $\hat{F}_L(v_{abth}^{k+1}\hat{v}_\alpha^{k,k+1}, t_{k+1})$ according to the process of mapping (75)
  3 Calculate Shkarofsky's integrals according to Eqs. (72)-(73)
  4 Compute the amplitudes of Rosenbluth potentials according to Eqs. (28)-(29)
  5 Update derivatives of Rosenbluth potential's amplitudes according to Eqs. (133)-(135)
  6 Calculate normalized FPRS collision operator, $\hat{\mathfrak{C}}_{ab}(\hat{v}_\alpha^{k,k+1}, t_{k+1})$ according to Eq. (89)
  7 Update the amplitudes $\hat{\mathfrak{C}}_{lab}(\hat{v}_\alpha^{k,k+1}, t_{k+1})$ according to Eq. (88)

Upon discretization, implicit methods for the FPRS collision equation lead to a complex system of nonlinear algebraic equations, necessitating an effective nonlinear solver strategy for its solution. In this study, we rely on the King method for this task. Under

the assumption that the characteristic parameters are independent of l, the lth-order amplitude function of species a at the αth node and $(k+1)^{th}$ time level within k^{th} time block will be smoothed by KFE (52), reads:

$$\hat{f}_l(\hat{v}_\alpha^{k,k+1}, t_{k+1}) = \frac{2\pi}{\pi^{3/2}} \sum_{s=1}^{N_{K_a}} \left[\hat{n}_{a_s}^{k+1} \mathcal{K}_l \left(\hat{v}_\alpha^{k,k+1}; \hat{u}_{a_s}^{k+1}, \hat{v}_{ath_s}^{k+1} \right) \right], \quad 0 \le l \le l_{max}. \quad (90)$$

The characteristic parameters are determined by solving the CPEs (53), at $(k+1)^{th}$ time level within k^{th} time block, as given by:

$$\hat{\mathcal{M}}_{j,l}(t_{k+1}) = \begin{cases} C_M{}^l_j \sum\limits_{s=1}^{N_{K_a}} \hat{n}_{a_s}^{k+1} \left(\hat{v}_{ath_s}^{k+1} \right)^j \left(\dfrac{\hat{u}_{a_s}^{k+1}}{\hat{v}_{ath_s}^{k+1}} \right)^l \left[1 + \sum\limits_{i=1}^{j/2} C^i_{j,l} \left(\dfrac{\hat{u}_{a_s}^{k+1}}{\hat{v}_{ath_s}^{k+1}} \right)^{2i} \right], & l = 0, \\[4ex] C_M{}^l_j \sum\limits_{s=1}^{N_{K_a}} \hat{n}_{a_s}^{k+1} \left(\hat{v}_{ath_s}^{k+1} \right)^j \left(\dfrac{\hat{u}_{a_s}^{k+1}}{\hat{v}_{ath_s}^{k+1}} \right)^l \left[1 + \sum\limits_{i=1}^{(j-1)/2} C^i_{j,l} \left(\dfrac{\hat{u}_{a_s}^{k+1}}{\hat{v}_{ath_s}^{k+1}} \right)^{2i} \right], & l = 1, \end{cases} \quad (91)$$

where j satisfies the collection of (j, l) provided in Sec. 3.2.2. Here, the normalized kinetic moment calculated using Romberg integral (69) at the $(k+1)^{th}$ time level within k^{th} time block can be formulated as:

$$\hat{M}_{j,l}(t_{k+1}), Error\left(\hat{M}_{j,l}(t_{k+1}) \right) = \left\langle ([\hat{v}_\alpha^{k,k+1}])^j \,|\, \hat{f}_l([\hat{v}_\alpha^{k,k+1}], t_{k+1}) \right\rangle_R. \quad (92)$$

Algorithm 5 Calculating the FPRS collision operator of species a at the $(k+1)^{th}$ time level within k^{th} time block

---

From inputs Δ_{t_k}, $l_M(t_{k+1})$, $N_{K_a}(t_{k+1})$,$\hat{v}_\alpha^{k,k+1}$, collection of (j, l) and $f_l(\hat{v}_\alpha^{k,k+1}, t_{k+1})$
1 Update n_a^{k+1}, I_a^{k+1}, K_a^{k+1}
2 Update $\hat{f}_l(\hat{v}_\alpha^{k,k+1}, t_{k+1})$ according to Eq. (77) for all species
For $a = 1, 2, \cdots, N_s$
For $b = a, 2, \cdots, N_s$
   3 Evaluate $\hat{\mathfrak{C}}_{lab}(\hat{v}_\alpha^{k,k+1}, t_{k+1})$ according to Algorithm 4
   If Conservation enforcing == **True**
     4A Update $\frac{\partial}{\partial t} n_a^{k+1}$, $\frac{\partial}{\partial t} I_a^{k+1}$, $\frac{\partial}{\partial t} K_a^{k+1}$ according to conservation enforcing algorithm 6
   Else
     4B Update $\frac{\partial}{\partial t} n_a^{k+1}$, $\frac{\partial}{\partial t} I_a^{k+1}$, $\frac{\partial}{\partial t} K_a^{k+1}$ according to Eqs. (44)-(46)
   End
End (for species b)
End (for species a)
5 Calculate total derivatives of conserved moments respective to t: $\frac{\partial}{\partial t} n_a^{k+1}$, $\frac{\partial}{\partial t} I_a^{k+1}$, $\frac{\partial}{\partial t} K_a^{k+1}$
6 Compute $\mathfrak{C}_l(\hat{v}_\alpha^{k,k+1}, t_{k+1})$ according to Eq. (87)
7 **Return** $\frac{\partial}{\partial t} n_a^{k+1}$, $\frac{\partial}{\partial t} I_a^{k+1}$, $\frac{\partial}{\partial t} K_a^{k+1}$, $\hat{v}_\alpha^{k,k+1}$ and $\mathfrak{C}_l(\hat{v}_\alpha^{k,k+1}, t_{k+1})$

To properly address those nonlinear algebraic equations described by Eqs. (86)-(92), it is imperative to impose constraints for ensuring conservation properties. By employing the Romberg integration with appropriate field nodes, we are able to achieve high-precision values for moments, including number density, momentum and energy. Build-

ing upon these high-precision values, according to manifold theory, we rely on backward error analysis to guarantee exact conservation. This is accomplished in Sec. 4.2.

4.2 Conservation enforcing

The accuracy of integrals (44)-(46) can be guaranteed for at least one during two-species collision processes (details in Sec. 5.1). The convergence criterion for conservation with high accuracy in two-species collision processes at the $(k+1)^{th}$ time level within k^{th} time block can be expressed as:

$$\min(\delta_t \hat{C}_a^{k+1}, \delta_t \hat{C}_b^{k+1}) \quad \ll \quad 1, \tag{93}$$

where

$$\delta_t \hat{C}_a^{k+1} \;=\; \left| Error(\delta_t \hat{n}_a^{k+1}) \right| + \left| Error(\delta_t \hat{I}_a^{k+1}) \right| + \left| Error(\delta_t \hat{K}_a^{k+1}) \right| \tag{94}$$

and similar for $\delta_t \hat{C}_b^{k+1}$. The aforementioned criterion will also be employed to evaluate the quality of field nodes as described in Sec. 3.2.4. Note that this current research will not utilize a self-adaptive scheme for (n_2, N_0).

From manifold theory[41] , post-step projection onto manifolds maintains a consistent convergence rate, and conservation properties can be preserved as long as the local solution errors remain sufficiently small. Consequently, incorporating a conservation strategy into our algorithm becomes feasible. This strategy enforces discrete conservation equations (48)-(50), by utilizing the more precise integrals, such as those for species b described by Eqs. (44)-(46), to provide more accurate representations during two-species collision processes. The convergence of this conservation strategy will occur when the criterion given by Eq. (93) is satisfied.

According to the conservation constraints represented by Eqs. (49)-(50), by applying relations (44)-(46), the rates of momentum and energy change of species a with respect to time at the $(k+1)^{th}$ time level can be theoretically expressed as:

$$\frac{\partial}{\partial t} I_a^{k+1} \;=\; -\frac{\partial}{\partial t} I_b^{k+1}, \quad \frac{\partial}{\partial t} K_a^{k+1} \;=\; -\frac{\partial}{\partial t} K_b^{k+1} \,. \tag{95}$$

When enforcing conservation (44), all rates of change in number density will be zero, yields:

$$n_a^{k+1} \;=\; n_a^k. \tag{96}$$

However, it is not feasible to achieve an exact numerical realization of Eq. (95) using a general integral scheme, such as Romberg integral. When all the local errors , represented by $Error\left(\delta_t \hat{I}^{k+1}\right)$ and $Error\left(\delta_t \hat{K}^{k+1}\right)$ are sufficiently small through the utilization of appropriate field nodes determined by (n_2, N_0), we can enforce Eq. (95) by selecting the more precision one between species a and species b. For example, if the local errors of species b are small, $\delta_t \hat{C}_a^{k+1} \geq \delta_t \hat{C}_b^{k+1}$, then according to manifold theory, let

$$\frac{\partial}{\partial t} I_a^{k+1} \;:=\; -\frac{\partial}{\partial t} I_b^{k+1}, \quad \frac{\partial}{\partial t} K_a^{k+1} := -\frac{\partial}{\partial t} K_b^{k+1} \tag{97}$$

at each stage of the $(k+1)^{th}$ time level within k^{th} time block.

In the trapezoidal method, the values of momentum and energy at the $(k+1)^{th}$ time

level within k^{th} time block are calculated through an implicit iteration, for species a, can be expressed in the following form:

$$I_a^{k+1} = I_a^k + \frac{1}{2}\Delta_{t_k}\left(\frac{\partial}{\partial t}I_a^k + \frac{\partial}{\partial t}I_a^{k+1*}\right), \quad K_a^{k+1} = K_a^k + \frac{1}{2}\Delta_{t_k}\left(\frac{\partial}{\partial t}K_a^k + \frac{\partial}{\partial t}K_a^{k+1*}\right). \quad (98)$$

The implicit iteration at each time level will be terminated when the thermal velocity of all plasma species at the ith stage of $(k+1)^{th}$ time level within k^{th} time block satisfies the following condition, for species a reads:

$$\left|\frac{v_{ath}(t_{k+1_i})}{v_{ath}(t_{k+1_{i-1}})} - 1\right| \le 10^{-6}, \quad i \ge 2. \quad (99)$$

Consequently, the average velocity and thermal velocity of species a at the $(k+1)^{th}$ time level within k^{th} time block can be expressed as:

$$u_a^{k+1} = \frac{I_a^{k+1}}{\rho_a^{k+1}}, \quad v_{ath}^{k+1} = \sqrt{\frac{2}{3}\left[\frac{2K_a^{k+1}}{\rho_a^{k+1}} - (u_a^{k+1})^2\right]}. \quad (100)$$

Thus, the normalized average velocity of species a is calculated as $\hat{u}_a^{k+1} = u_a^{k+1}/v_{ath}^{k+1}$. By applying Eqs. (58)-(60), we obtain:

$$\hat{\mathcal{M}}_{0,0}(t_{k+1}) \equiv 1, \quad (101)$$

$$\hat{\mathcal{M}}_{1,1}(t_{k+1}) = 3\hat{u}_a^{k+1}, \quad (102)$$

$$\hat{\mathcal{M}}_{2,0}(t_{k+1}) = \frac{3}{2} + \left(\hat{u}_a^{k+1}\right)^2. \quad (103)$$

The conservation enforcing algorithm is presented in the following pseudo-code (6).

Algorithm 6 Enforcing conservation during two-species collision processes at each stage of $(k+1)^{th}$ time level within k^{th} time block.

From inputs $\hat{\mathfrak{C}}_{lab}(\hat{v}_\alpha^{k,k+1}, t_{k+1})$ of species a and species b:

1 Evaluate $\hat{\mathcal{R}}_{j,l}(t_{k+1})$ and $Error\left(\hat{\mathcal{R}}_{j,l}(t_{k+1})\right)$ by calculating the Romberg integral (70)

2 Update $\frac{\partial}{\partial t}n^{k+1}$, $\frac{\partial}{\partial t}I^{k+1}$, $\frac{\partial}{\partial t}K^{k+1}$ for species a and species b according to Eqs. (44)-(46)

3 Evaluate whether $\min(\delta_t\hat{C}_a^{k+1}, \delta_t\hat{C}_b^{k+1}) \ll 1$ (give in Eq. (93))

If $\delta_t\hat{C}_a^{k+1} \ge \delta_t\hat{C}_b^{k+1}$

  4A $\frac{\partial}{\partial t}I_a^{k+1} := -\frac{\partial}{\partial t}I_b^{k+1}$, $\frac{\partial}{\partial t}K_a^{k+1} := -\frac{\partial}{\partial t}K_b^{k+1}$

Else

  4B $\frac{\partial}{\partial t}I_b^{k+1} := -\frac{\partial}{\partial t}I_a^{k+1}$, $\frac{\partial}{\partial t}K_b^{k+1} := -\frac{\partial}{\partial t}K_a^{k+1}$

End

5 Let $\frac{\partial}{\partial t}n^{k+1} := 0$ for all species

6 **Return** $\frac{\partial}{\partial t}n^{k+1}$, $\frac{\partial}{\partial t}I^{k+1}$, $\frac{\partial}{\partial t}K^{k+1}$ for all species.

By implementing the conservation enforcing scheme mentioned above, the accuracy of the conservation (48)-(50) are determined by the precision of the more accurate species rather than the less accurate one. It is worth noting that small local solution errors of $\delta_t\hat{n}$ (44), $\delta_t\hat{I}$ (45) and $\delta_t\hat{K}$ (46) for at least one species during two-species Coulomb col-

lision process, represented by Eq. (93), are a necessary condition for convergence. This condition is verified at each stage and every time level in our algorithm. Finally, the main procedure for solving FPRS collision spectrum equation by utilizing trapezoidal scheme at the $(k+1)^{th}$ time level within k^{th} time block is outlined in the Algorithm 7.

Algorithm 7 Solving FPRS collision spectrum equation by utilizing trapezoidal scheme at the $(k+1)^{th}$ time level within k^{th} time block

---

From inputs Δ_{t_k}, $\hat{v}_\alpha^k$, $l_M(t_k)$, $N_{K_a}(t_k)$, collection of (j,l) and $f_l(\hat{v}_\alpha^k, t_k)$ for all species
Initial $N_{iter} = 1$ and denote $X = n, I, K$
1 Compute $\frac{\partial}{\partial t} X_a^k$, $\mathfrak{C}_l(\hat{v}_\alpha^k, t_k)$, v_{ath}^{k+1*}, $\hat{v}_\alpha^{k,k+1*}$ and $f_l(\hat{v}_\alpha^{k,k+1*}, t_{k+1})$ according to Algorithm 3
For $N_{iter} = 2, 3, \cdots, N_{in}$
    2 Update $\frac{\partial}{\partial t} X_a^{k+1*}$, $\hat{v}_\alpha^{k,k+1*}$ and $\mathfrak{C}_l(\hat{v}_\alpha^{k,k+1*}, t_{k+1})$ according to Algorithm 5
    3 Let $\mathfrak{C}_l(\hat{v}_\alpha^{k,k+1*}, t_{k+1}) = \frac{1}{2}[\mathfrak{C}_l(\hat{v}_\alpha^k, t_k) + \mathfrak{C}_l(\hat{v}_\alpha^{k,k+1*}, t_{k+1})]$
    4 Let $\frac{\partial}{\partial t} X_a^{k+1} = \frac{1}{2}[\frac{\partial}{\partial t} X_a^k + \frac{\partial}{\partial t} X_a^{k+1*}]$
    5 Evaluate $f_l(\hat{v}_\alpha^{k,k+1*}, t_{k+1})$ according to Eq. (81)
    6 Calculate X_a^{k+1} according to Eq. (82)
    7 Compute v_{ath}^{k+1} according to Eq. (100)
    8 Calculate $\hat{f}_l(\hat{v}_\alpha^{k,k+1*}, t_{k+1})$ according to Eq. (77)
    9 Smooth $\hat{f}_l(\hat{v}_\alpha^{k,k+1*}, t_{k+1})$ utilizing King method according to Algorithm 1
    10 Update $\hat{v}_\alpha^{k,k+1} = \hat{v}_\alpha^{k,k+1*} v_{ath}^{k+1*}/v_{ath}^{k+1}$ and $f_l(\hat{v}_\alpha^{k,k+1}, t_{k+1})$ according to Eq. (82)
    11 **If** Eq. (99) == **True Break Else** $v_{ath}^{k+1*} = v_{ath}^{k+1}$ and $\hat{f}_l(\hat{v}_\alpha^{k,k+1*}, t_{k+1}) = \hat{f}_l(\hat{v}_\alpha^{k,k+1}, t_{k+1})$ **End**
End
12 Update $\hat{v}_\alpha^{k+1}$ determined by $\hat{v}_M$, (n_2, N_0) and $f_l(\hat{v}_\alpha^{k,k+1*}, t_{k+1})$ for $(k+1)^{th}$ time block

---

4.3 Timestep

The Coulomb collision process encompasses multiple dynamical times-scales (such as inter-species time-scale, self-collision time-scale, relaxation time-scale of conserved moments, et al.), making it stiff. In this paper, a timestep of $\Delta t = 2^{-5}$ (unless otherwise stated) is utilized for fixed timestep cases. Self-adaptive timestep will be employed (unless otherwise stated) to improve the algorithm performances, which is determined by the following algorithm:

$$\Delta_{t_{k+1}} = \min\left(ratio_{dt_k} \times \Delta_{t_k}, ratio_{M_j} \times \left|\frac{1}{y^k}\frac{\partial y^k}{\partial t}\right|\right). \tag{104}$$

Here, the subscripts k denotes the time level and y represents momentum I and total energy K for all species. $\Delta_{t_k} = 1$ at the initial time level. Parameters $ratio_{dt_k}$ and $ratio_{M_j}$ are given constants, with default values of $ratio_{dt_k} = 1.1$ and $ratio_{M_j} = 0.01$ in this paper. For cases utilizing self-adaptive timestep, nearly all timesteps satisfy $10^{-3} \leq \Delta t \leq 0.1$.

As a contrast, the explicit timestep size determined by the CFL condition[2] is calculated as follows:

$$\Delta_{t_0}^{Exp} = R_{CFL} \times \min_{\substack{l=0,1,\cdots,l_M \\ a,b=1,2,\cdots,N_s}}\left\{\frac{\Delta\hat{v}}{A_{lab}}, \frac{(\Delta\hat{v})^2}{D_{lab}}\right\}. \tag{105}$$

In this equation, the parameter $R_{CFL} = 0.1$ is utilized in explicit method to ensure long-

term stability. Additionally, A_{lab} and D_{lab} represent the transport coefficients in the FPRS collision operator (give in Eq. (3)), reads:

$$A_{lab} = \frac{n_a}{v_{ath}^3}\frac{n_b}{v_{bth}^3} \times C_{\hat{H}}\Gamma_{ab}\frac{\partial}{\partial \hat{v}_{ab}}\hat{H}_L, \quad D_{lab} = \frac{n_a}{v_{ath}^3}\frac{n_b}{v_{bth}^3} \times C_{\hat{G}}\Gamma_{ab}\frac{\partial^2}{\partial \hat{v}_{ab}^2}\hat{G}_L . \quad (106)$$

This explicit timestep size (105) will not be directly utilized in our algorithm, but rather serve as a reference for our timestep represented by Eq. (104).

5 Numerical results

In order to demonstrate the convergence and effectiveness of our method for solving the FPRS collision equation (17), we will assess the performance of our algorithm with various examples of different degrees of complexity. In the benchmarks conducted in this session, the initial distribution functions for particles at $t = 0$ are drifting Maxwellian distributions with a specified number density n_a, average velocity u_a and temperature T_a, which can be written as:

$$f(\hat{\mathbf{v}}, t) = \frac{n_a}{v_{ath}^3}\hat{f}(\hat{\mathbf{v}}, t) = \frac{1}{\pi^{3/2}}\frac{n_a}{v_{ath}^3}\sum_{s=1}^{N_{K_0}}\left[\frac{\hat{n}_{a_s}}{(\hat{v}_{ath_s})^3}\mathrm{e}^{-(\hat{\mathbf{v}}-\hat{u}_{a_s}\mathbf{e}_z)^2}\right] . \quad (107)$$

Note that the upright "e" represents the base of the natural logarithm, while the black body "e$_z$" denotes the basis vector of the z coordinate.

For all cases, all the parameters are normalized values with units defined in Sec.2. Unless otherwise specified, the default values for (n_2, N_0) are set to $(7,7)$ as specified in section 3.2.4 and initial number of King functions N_{K_0} is set to 1 at the initial time level. Hence, default values of parameters are $\hat{n}_{a_s} = \hat{v}_{ath_s} = 1$ and $\hat{u}_{a_s} = \hat{u}_a$. For L01jd2 scheme, number of King function is constant, $N_{K_a} \equiv N_{K_0}$, while according to limitations provided by Algorithm 2, $N_K^{min} \leq N_{K_a}(t) \leq N_K \leq N_K^{max}$, is specified in L01jd2NK and L01jd2nh schemes. The details are provided in Sec. 3.2.3. In this paper, the default solver is L01jd2NK scheme for scenarios where $max(m_M, 1/m_M) \sim 1$, and L01jd2 scheme for cases where $max(m_M, 1/m_M) \gg 1$ during collisions between electrons and ions.

5.1 Two-species thermal equilibration

In this instance, we demonstrate the convergence performance of our algorithm on two-species thermal equilibration, a widely used benchmark for evaluating schemes to solve the FPRS collision equation. The parameters for this case are $m_a = 2$, $m_b = 3$, $Z_a = Z_b = 1$, $n_a = n_b = 1$, $u_a = u_b = 0$, $T_a = 10$ and $T_b = 20$. Theoretically values for the temperature and momentum at equilibrium state can be obtained using conservation equations for momentum and energy:

$$I_s^k = \sum_a \left(m_a n_a^k u_a^k\right) \equiv \sum_a \left(m_a n_a^0 u_a^0\right), \quad (108)$$

$$K_s^k = \frac{1}{2}\sum_a \left[3n_a^k T_a^k + m_a n_a^k(u_a^k)^2\right] \equiv \frac{1}{2}\sum_a \left[3n_a T_a^0 + m_a n_a^0(u_a^0)^2\right] . \quad (109)$$

The initial total momentum and energy are $I_s^0 = 0$ and $K_s^0 = 45$ respectively. According to the conservation equations (108)-(109), the finial average velocity and temperatures of the thermal equilibrium state should be $u_\infty = 0$ and $T_\infty = 15$ respectively.

The zeroth-order two-species thermal equilibration model, as described by Bragin-

skii[60] , is presented through a semianalytical asymptotic temperature evolution equation:

$$\partial_t T_a = \nu_T^{ab} (T_a - T_b), \tag{110}$$

where the characteristic collision rate ν_T^{ab} is given by[48] :

$$\nu_T^{ab} \approx 441.72 \times \frac{\sqrt{m_a m_b} (Z_a Z_b)^2 n_b}{(m_a T_b + m_b T_a)^{3/2}} \ln \Lambda_{ab} . \tag{111}$$

The temperature relaxation time is defined as $\tau_T^{ab} = 1/\nu_T^{ab}$. The characteristic time τ_0 is equivalent to the initial temperature relaxation time unless otherwise specified.
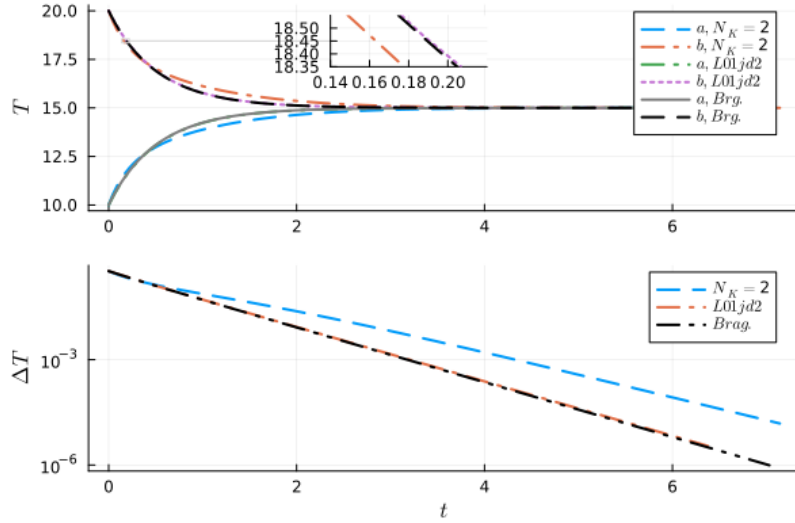
Figure 4: Two-species temperature equilibration with fixed timestep, $\Delta t = 2^{-5}$: Temperatures (upper) and relative disparity of temperatures (lower), $\Delta T = \left| T_a^k - T_b^k \right| / \left(T_a^k + T_b^k \right)$ as functions of time. The color lines represent the numerical solution while the gray and black lines represent the Braginskii's values.

The semianalytical equation (110) is solved employing the standard explicit Runge-Kutta[45] method of order 4, and the results are depicted in Fig. 4. The temperatures are plotted as functions of time and compared against the numerical solution of our kinetic model with a fixed timestep of $\Delta t = 2^{-5}$ and L01jd2NK scheme with the maximum number of King function $N_K = 2$. Fig. 4 demonstrates excellent agreement between our fully kinetic model and the semianalytical solution. Furthermore, upon comparing the results of L01jd2 ($N_{K_a}(t) \equiv 1$ in this case) and L01jd2NK ($N_K = 2$) with the semianalytical solution, it is observed that the temperature decay rate of L01jd2NK is a slightly faster than that of Braginskii's within the initial time block ($t < 0.58$ in this case), but this trend reverses when $t \geq 0.58$ (Similar to the behavior observed in the FVM's approach as shown in the Fig.14 of Ref.[2]). However, the results of L01jd2 scheme strictly adhere to the semianalytical solution, as shown in the lower subplot of Fig. 4.

The solid line in Fig. 5 depicts the relative deviation of temperature between our kinetic model and reference values T_{ref}, given by $RDT = |T_{kin} - T_{ref}| / T_{ref}$ at $t = 0.5$, as a function of the fixed timestep, Δt. The reference value, T_{ref}, is computed using a sufficiently small timestep, $\Delta t = 2^{-11}$, in our kinetic model. The results indicate that our algorithm exhibits 2nd-order convergence in time discretization.

25
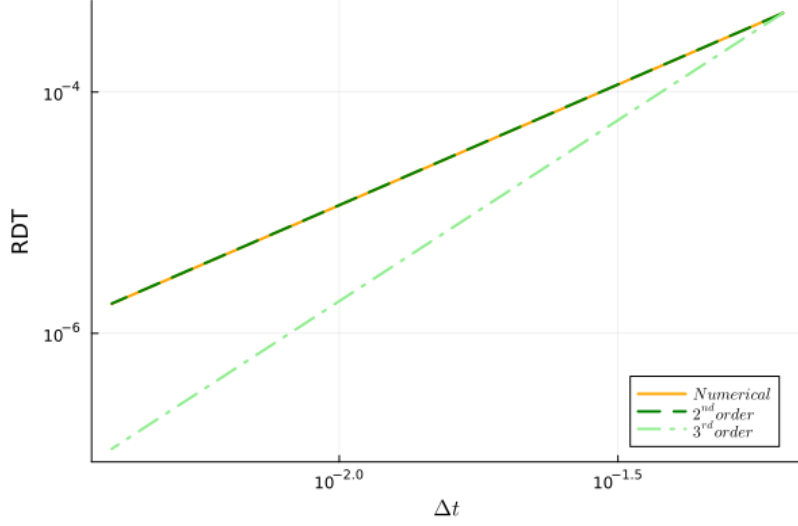
Figure 5: Two-species temperature equilibration with fixed timestep, Δt: Demonstration of second-order convergence of the time discretization scheme.
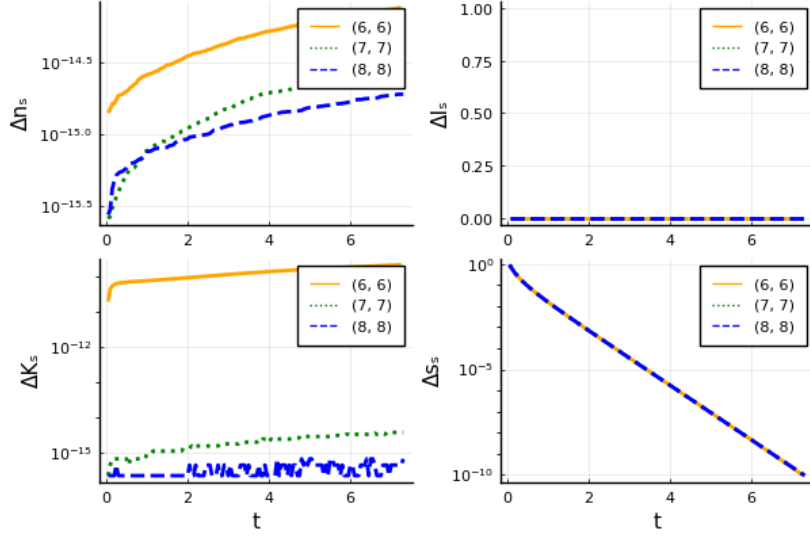
Figure 6: Two-species temperature equilibration without enforcing conservation: Discrete conservation errors as functions of time and number of field nodes, (n_2, N_0).

The temporal evolution of errors in the conserved quantities, specifically discrete number (or mass) density, momentum, energy conservation,

$$\Delta n_s(t_k) = (N_s)^{-1} \sum_a \left| n_a^k/n_a^0 - 1 \right|, \tag{112}$$

$$\Delta I_s(t_k) = \left| I_s^k/I_s^0 - 1 \right|, \tag{113}$$

$$\Delta K_s(t_k) = \left| K_s^k/K_s^0 - 1 \right|, \tag{114}$$

and entropy conservation,

$$\Delta s_s(t_k) = \left(s_s^k - s_s^{k-1} \right) / \left[\Delta t \left(s_s^k + \delta s_s \right) \right] \tag{115}$$

26

are depicted in Fig. 6 for varying number of field nodes with (n_2, N_0). Here, the parameter δs_s is given by $\delta s_s = \delta_\zeta^{-1}(|s_s^0| + |s_s^{end}|)$, where $\zeta = |s_s^0 s_s^{end}| / (s_s^0 s_s^{end})$ and s_s^{end} are the value of s_s at the finial time level. $\delta s_s \equiv 0$ in all cases except for the last one in Sec. 5. Since entropy conservation serves as a convergence criterion for our algorithm, a first-order implicit scheme is utilized to calculate the entropy change, as defined by Eq. (115).

The discrete mass conservation is achieved with high precision for all given (n_2, N_0), even without enforcing conservation. The discrete momentum conservation and H-theorem are preserved all the time. The discrete error of the energy conservation rapidly decreases with an increase of number of field nodes and reaches the level of round-off error when $(n_2, N_0) = (8, 8)$, corresponding to a total number of nodes $N_n = 257$. Since $l_{M_1} = 1$ for two-species temperature equilibration, the total number of field nodes is $N_{v2} = l_{M_1} \times N_v = 1793$ for Rosenbluth potentials step 3.1.2. The results of ΔK_s in Fig. 6 indicate that the convergence order of the velocity-space discretization scheme is about 16. The convergence order[61] of a discrete algorithm is evaluated using:

$$order \;\; = \;\; [1/\log(2)]\log(\epsilon_{n_2-1}/\epsilon_{n_2}) \,. \tag{116}$$

Here, we assume that $\epsilon_{n_2} = \mathcal{O}[(h_{n_2})^{order}]$, where h_{n_2} represents the grid size with grid number is $2^{n_2} + 1$. The number of time levels in this case is determined to be $N_t = 122$, based on the termination condition $\Delta s_s \leq 10^{-10}$.
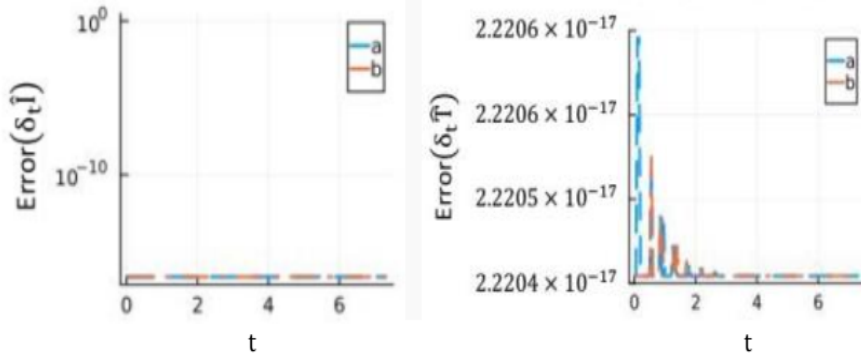
Figure 7: Two-species temperature equilibration without enforcing conservation: Romberg integral errors of $\delta_t \hat{I}$ and convergence criterion $\delta_t \hat{T}$ respect to time t when $(n_2, N_0) = (7, 7)$.

The relative errors of Romberg integrals for the first few orders of $\hat{\mathcal{R}}_{j,l}$ (42), $\delta_t \hat{n}_a$ (44), $\delta_t \hat{I}_a$ (45), $\delta_t \hat{K}_a$ (46) and convergence criterion $\delta_t \hat{T}_a$ (47) during two-species Coulomb collisions are depicted in Fig. 7 and Fig. 8 when $(n_2, N_0) = (7, 7)$. It is evident that all the relative errors are at the level of round-off error. The maximal errors occur at the initial moment and diminish to the level of round-off error over a collision time scale. The fact that convergence criterion $\delta_t \hat{T}_a$ consistently equals the theoretical value indicates that our algorithm exhibits strong convergence properties.

The relationship between relative errors and orders (n_2, N_0) is depicted in Fig. 8. In all cases, the relative errors are significantly smaller that one, indicating that condition (give in Eq. (93)) is consistently satisfied. Specifically, the relative errors of species a remain at the level of round-off error throughout. However, the orange solid line representing species b in Fig. 8 reveals that both the relative errors of $\delta_t \hat{n}_b$ and $\delta_t \hat{K}_b$ are two orders of magnitude larger than the round-off error when $(n_2, N_0) = (6, 6)$ at initial moments. This discrepancy can result in discrete errors in energy conservation (see Fig. 6). Furthermore, Fig. 8 also indicates that as the number of grids (n_2, N_0) increases, the errors of species b

27

rapidly decrease to the level of round-off error. This suggests that integrals (44)-(46) will be accurate at least for one species during two-species collision process and the integration accuracy for any less accurate species can be improved by refining field nodes.
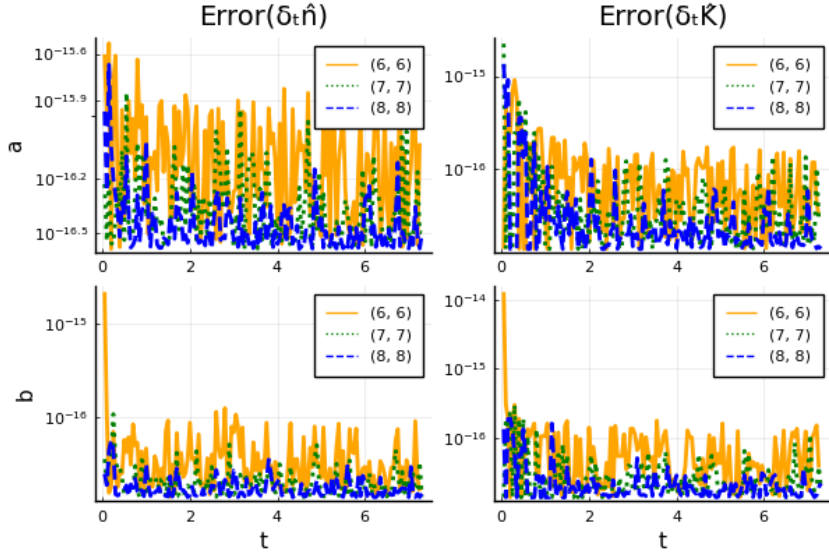

Figure 8: Two-species temperature equilibration without enforcing conservation: Romberg integral errors of $\delta_t\hat{n}$ and $\delta_t\hat{K}$ respect to time for collision species a and b with various (n_2, N_0).
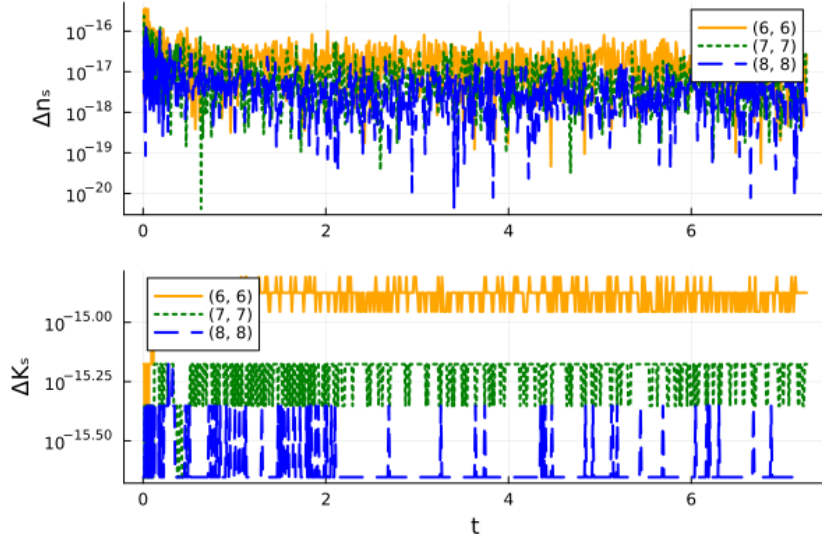

Figure 9: Two-species temperature equilibration with enforcing conservation: Discrete conservation errors as functions of time and number of field nodes, (n_2, N_0).

When implementing the conservation enforcing algorithm 6, the time histories of the associated conservation errors, Δn_s and ΔK_s are plotted in Fig. 9 for varying number of field nodes, (n_2, N_0). As anticipated, precise discrete conservation can be achieved for all given (n_2, N_0).

28

We can also demonstrate second-order time convergence of the trapezoidal scheme by computing the L_2-norm of relative difference in solution compared to a reference solution,

$$L_2^{\Delta t} = \sqrt{\langle f_l^{\Delta t}/f_l^{\Delta t_{ref}} - 1, f_l^{\Delta t}/f_l^{\Delta t_{ref}} - 1 \rangle} . \tag{117}$$

Here, $f_l^{\Delta t_{ref}}$ is the solution obtained using a reference timestep size, $\Delta t_{ref} = 2^{-11}$; refer to Fig. 10 (upper) when $(n_2, N_0) = (7, 7)$. As expected, second-order convergence is realized with the refinement of Δ_t. The CPU time as a function of Δt when $(n_2, N_0) = (7, 7)$ is also plotted in the lower subplot of Fig. 10. The total solution time scales approximately as $\mathscr{O}(1/\Delta t)$. This first-order correlation arises from the rapid convergence of implicit iteration, typically requiring only a few iterations even with different timesteps , as demonstrated by Fig. 23 in Sec. 5.4. Compared to the explicit timestep, $\Delta_t^{Exp} \approx 1.5 \times 10^{-3}$ in this case estimated by Eq. (105), a timestep greater than one or two order of magnitude can be used in our algorithm with acceptable time-discrete precision.
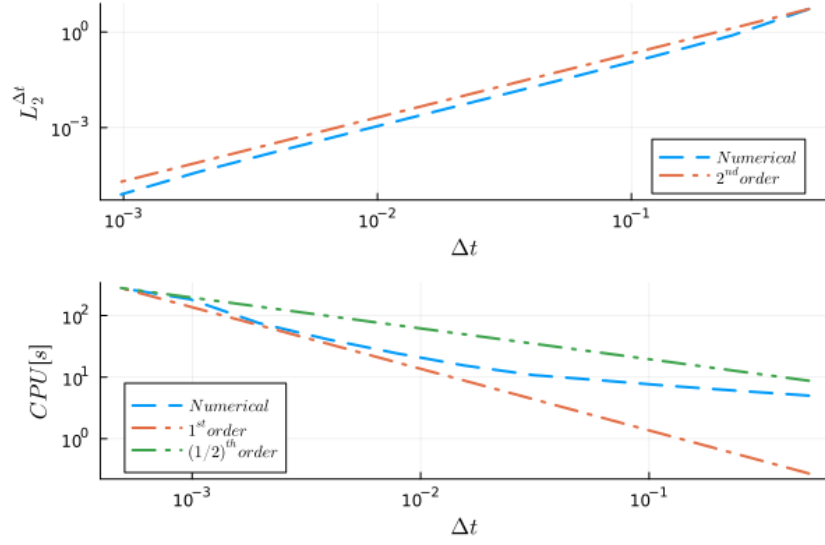
Figure 10: Two-species temperature equilibration with fixed timestep, Δt: Demonstration of 2th-order convergence of time discretization scheme in L_2-norm and the CPU time as function of timestep, Δt.

Fig. 11 illustrates the time discretization errors of the non-conserved moments, $\Delta \hat{\mathcal{M}}_{j,l}$ as functions of time with various j when $j \geq 4$. Here, $\Delta t = 2^{-5}$, $N_K = 2$ and $(n_2, N_0) = (7, 7)$. The quantity $\Delta \hat{\mathcal{M}}_{j,l}$, which is more effective than $\delta \hat{\mathcal{M}}_{j,l}$ presented by Eq. (56), is defined as:

$$\Delta \hat{\mathcal{M}}_{j,l} = \left| \hat{M}_{j,l}(t_{k+1}) - \hat{\mathcal{M}}_{j,l}(t_{k+1}) \right| / \left| \hat{\mathcal{M}}_{j,l}(t_{k+1}) - \hat{M}_{j,l}(t_k) \right|, \tag{118}$$

which measures the relative error resulting from velocity discretization during optimization process. Notes that the symbols $\hat{M}_{j,l}$ and $\hat{\mathcal{M}}_{j,l}$ represent the normalized kinetic moment, which are computed from the amplitude function before (give in Eq. (38)) and after (give in Eq. (53)) being smoothed by King function, respectively. By applying Eqs. (58)-(60) in L01jd2NK scheme, the time discretization errors of the conserved moments, $\Delta \hat{\mathcal{M}}_{j,l}$ given by Eq. (118), for all species are exactly zero. Furthermore, convergence of the optimization of $(j, l)^{th}$-order normalized kinetic moments is achieved when $\Delta \hat{\mathcal{M}}_{j,l} \leq rtol_{NK}$,

where $rtol_{NK}$ is a given relative tolerance. In this study, we set parameter $rtol_{NK}$ to 10^{-11} unless otherwise specified. As shown in Fig. 11, the moment with order $j = 6$ exhibits a maximum deviation not exceeding 6.6% for all species under consideration when $N_K = 2$. Additionally, the time discretization errors for the convergent order, $j = 4$, are generally no greater than 10^{-11}.
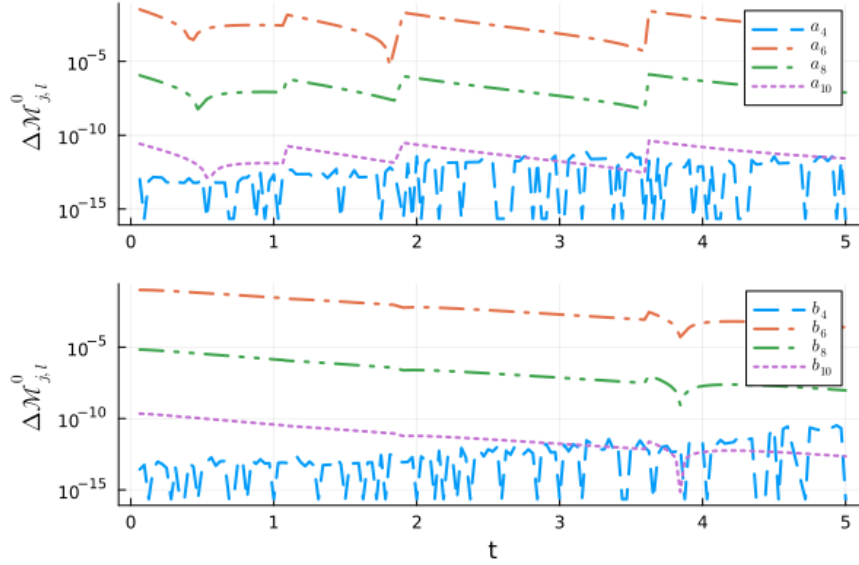

Figure 11: Two-species temperature equilibration without enforcing conservation: Time discretization errors of the non-conserved moments as functions of time with various j when $\Delta t = 2^{-5}$, $N_K = 2$ and $(n_2, N_0) = (7, 7)$.
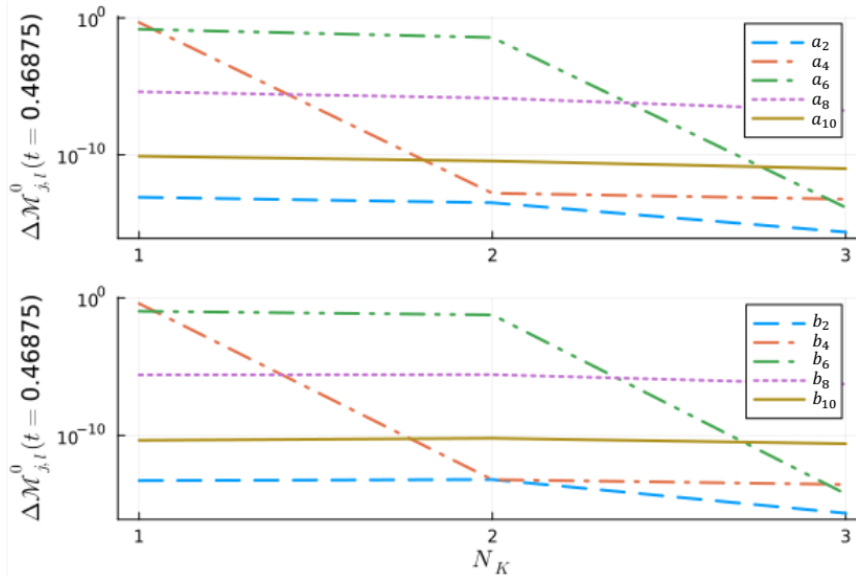
Figure 12: Two-species temperature equilibration without enforcing conservation: Time discretization errors of the non-conserved moments as functions of N_K with various j when $\Delta t = 2^{-6}$, $t_k \approx 0.47$ and $(n_2, N_0) = (8, 8)$.

The high-order moment convergence property of the present method is further investigated. Fig. 12 illustrates the time discretization errors of the non-conserved moments, $\Delta\hat{\mathcal{M}}_{j,l}$, at $t_k \approx 0.47$ as functions of N_K with various j. For this test, a refined timestep and field nodes, $\Delta t = 2^{-6}$ and $(n_2, N_0) = (8, 8)$ are utilized. As depicted in Fig. 12, all the discretization errors of the non-conserved moments, $\Delta\hat{\mathcal{M}}_{j,l}$, decrease as N_K increase. Furthermore, it is observed that the highest convergent order is $j = 2$ when $N_K = 1$, $j = 4$ when $N_K = 2$ and $j = 6$ when $N_K = 3$. Therefore, it can be concluded that King method (Sec. 3.2.1) is a moment convergence algorithm.
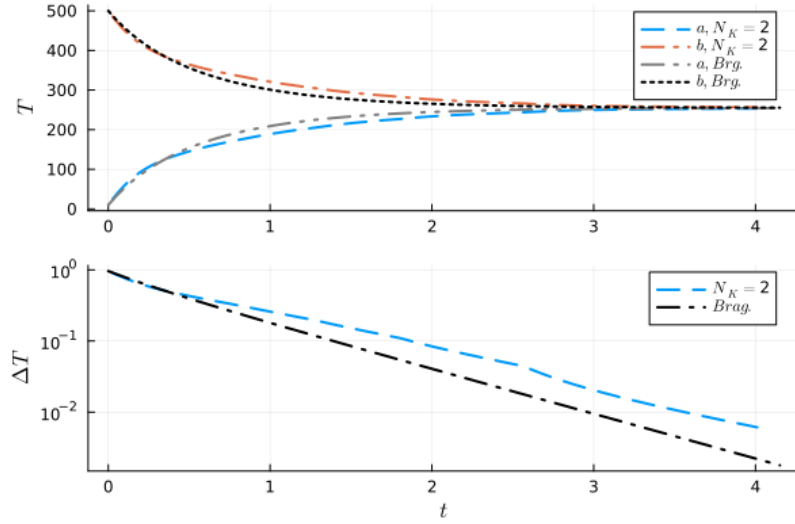
Figure 13: Two-species temperature equilibration with temperatures, $T_a = 10$, $T_b = 500$ and fixed timestep, $\Delta t = 2^{-5}$: When $N_K = 2$ and $(n_2, N_0) = (8, 7)$.
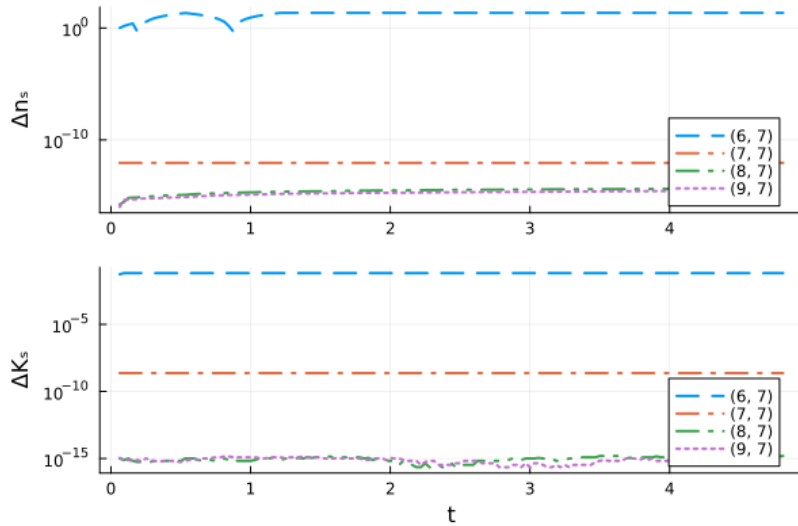
Figure 14: Two-species temperature equilibration with temperatures, $T_a = 10$, $T_b = 500$ and fixed timestep, $\Delta t = 2^{-5}$: Discrete conservation errors as functions of time and n_2 when $N_0 = 7$.

31

In situations with large thermal velocity disparity where $v_{th_f}/v_{th_s} \gg 1$, the maximum value of normalized speed $\hat{v}_M$ at $(k+1)^{th}$ time level within $(k+1)^{th}$ time block is determined by a more sophisticated method, for species a, can be described as follow:

$$\delta_l^0 \left(\hat{v}_M^{k+1}\right)^j \hat{f}_l(\hat{v}_M^{k+1}, t_{k+1}) + \delta_l^1 \left(\hat{v}_M^{k+1}\right)^{j+1} \left|\hat{f}_l(\hat{v}_M^{k+1}, t_{k+1})\right| = 4.44 \times 10^{-17}, \ j = 2.5 N_{K_a}. \quad (119)$$

Applying information at the $(k+1)^{th}$ time level within k^{th} time block and solving the above equation, the optimized value of $\hat{v}_M$ at $(k+1)^{th}$ time level within $(k+1)^{th}$ time block can be obtained. It is evident that $\hat{v}_M$ will vary across different time levels, while remaining constant within each time block. This step ensures that the value of distribution function at the right boundary of speed can be effectively disregarded as zero.

For example, when $T_a = 10$ and $T_b = 500$, with all other parameters remaining the same as in the previous case, the temperatures calculated by the L01jd2NK scheme using a fixed timestep of $\Delta t = 2^{-5}$, $N_K = 2$ and $(n_2, N_0) = (8, 7)$ are depicted as functions of time in Fig. 13. As anticipated, the results show good agreement between our fully kinetic model and the semianalytical solution. By comparing Fig. 14 and Fig. 6, we can see that achieving the same level of precision with an increased temperature difference requires more refined field nodes by increasing n_2.

5.2 Electron-Deuterium thermal equilibration

In order to verify the convergence in scenarios involving significant mass disparity, we examine the thermal equilibration between electron and Deuterium, denoted as slanted e and D respectively. The parameters $m_e = 1/1836$, $m_D = 2$, $-Z_e = Z_D = 1$, $n_e = n_D = 1$, $\hat{u}_e = \hat{u}_D = 0$, $T_e = 1$ and $T_D = 10$. In this instance, the final average velocity and temperatures of the thermal equilibrium state are expected to be $u_\infty = 0$ and $T_\infty = 5.5$ respectively. The L01jd2 scheme is employed for solving this case with a self-adaptive timestep. The total number of time levels, denoted as N_t, is 792, when the termination condition is $\Delta s_s \leq 10^{-8}$. We aim to demonstrate that L01jd2 scheme provides a reliable approximation of the fully kinetic model for situations characterized by large mass disparity.
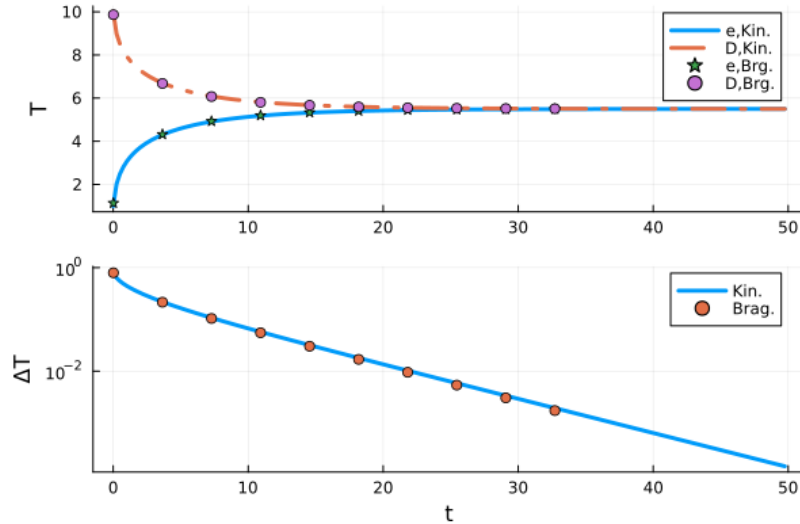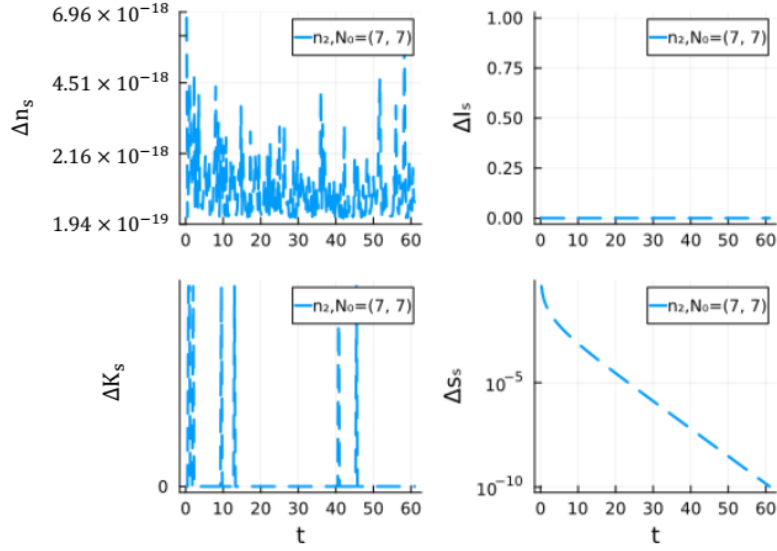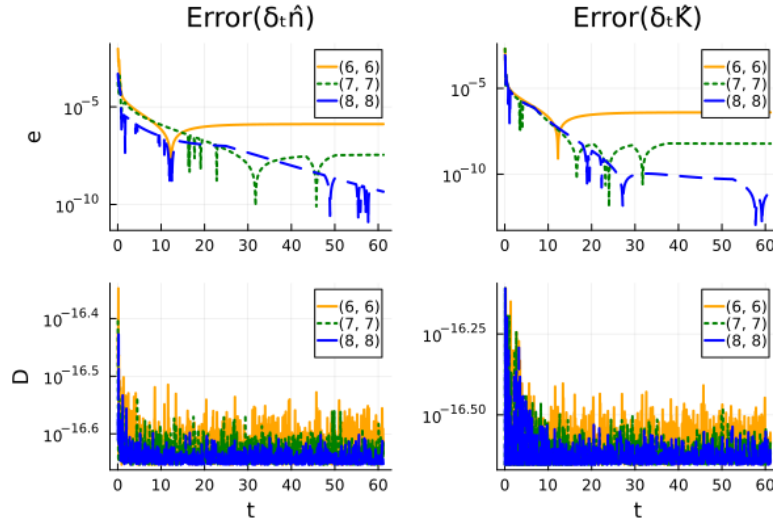

Figure 15: e-D thermal equilibration with enforcing conservation when solved by L01jd2 with fixed timestep, $\Delta t = 2^{-5}$: Average velocities and temperatures as function of time t when $(n_2, N_0) = (7, 7)$.

The temperatures of species e and D are presented as functions of time t in Fig. 15, demonstrating the attainment of correct equilibrium values. The temporal evolution of errors in discrete number density, momentum, energy conservation (112)-(114) and entropy conservation is illustrated in Fig. 16. Additionally, the local relative errors, $Error(\delta_t \hat{n})$ and $Error(\delta_t \hat{K})$ of species e and D are depicted in Fig. 17 when enforcing conservation. It can be observed that all errors of species D are at the level of round-off errors, which those for species e are acceptably small, aligning with the convergence criterion for conservation (give in Eq. (93)).

Figure 16: e-D thermal equilibration with enforcing conservation when solved by L01jd2 with fixed timestep, $\Delta t = 2^{-5}$: Discrete conservation errors as functions of time when $(n_2, N_0) = (7, 7)$.
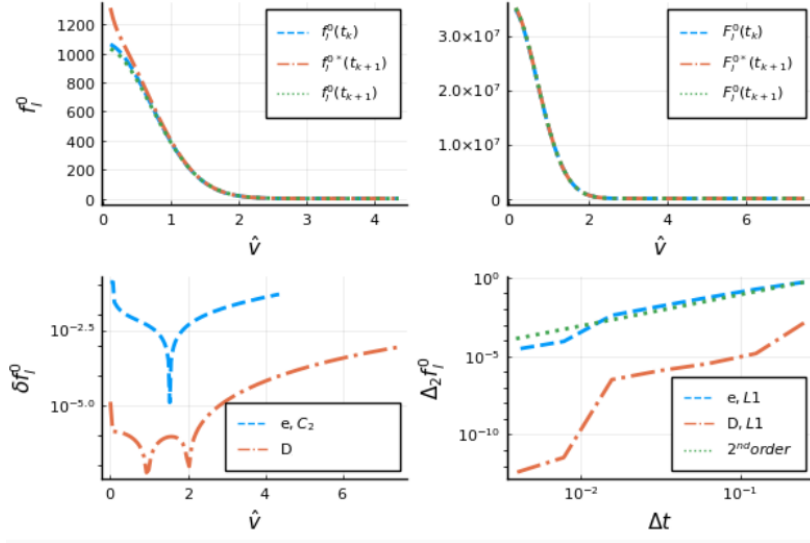

Figure 17: e-D thermal equilibration with enforcing conservation when solved by L01jd2 with fixed timestep, $\Delta t = 2^{-5}$: Local errors of $\delta_t \hat{n}$ and $\delta_t \hat{K}$ as functions of time with various (n_2, N_0).

To assess the effectiveness of L01jd2 in scenarios involving significant mass disparity,

we validate its convergence with the following criterion:

$$\Delta_0 f_l(\hat{v}_\alpha, t_{k+1}) \;\; = \;\; |f_l^*(\hat{v}_\alpha, t_{k+1}) - f_l(\hat{v}_\alpha, t_{k+1})| \,/\, |f_l^*(\hat{v}_\alpha, t_{k+1}) - f_l(\hat{v}_\alpha, t_k)| = C_0 \quad (120)$$

and

$$\Delta_2 f_l \;\; = \;\; (N_v)^{-1} \sum\nolimits_{\alpha=1}^{N_v} \delta f_l(\hat{v}_\alpha, t_{k+1}) \,. \tag{121}$$

Here,

$$\delta f_l(\hat{v}_\alpha, t_{k+1}) \;\; = \;\; |f_l^*(\hat{v}_\alpha, t_{k+1}) - f_l(\hat{v}_\alpha, t_{k+1})| \,/\, |\Delta t \times f_l^*(\hat{v}_\alpha, t_{k+1})| = C_2(\Delta t)^2 \,. \tag{122}$$

Functions $f_l^*(\hat{v}, t_{k+1})$ and $f_l(\hat{v}, t_{k+1})$ denote amplitudes before and after being smoothed by King function at the $(k+1)^{th}$ time level within k^{th} time block for species a, respectively.

Figure 18: e-D temperature equilibration with enforcing conservation when solved by L01jd2 with fixed timestep, $\Delta t = 2^{-5}$: Criterion C_2 (121) for situation with large mass disparity.

The convergence of function $\Delta_2 f_l$ is illustrated in Fig. 18, with a fixed finial time of $t_{k+1} = 0.5$. The right-lower subplot in Fig. 18 presents compelling evidence of the second-order accuracy convergence convergence of King method as Δt is refined. When using a sufficiently small timestep, such as $\Delta t = 0.01$, the maximum relative disparity of the distribution function before and after being smoothed by the King function does not exceed 11% for species e and 10^{-5} for species D in this scenario. This can be observed from the distribution function at k^{th} and $(k+1)^{th}$ time levels for species e and D in Fig. 18 (upper). The detailed relative disparity as a function of $\hat{v}$ is plotted in the left-lower subplot of Fig. 18 when $\Delta t = 2^{-5}$.

Similarly, the convergence of function $\Delta_0 f_l$ at the grid point $v_\alpha = 1.68 \times 10^{-2}$ is demonstrated in Fig. 19. The lower subplots show that the parameter C_0 tends to stabilize as a constant with the refinement of Δt at single speed node, i.e. $\hat{v}_\alpha = 0.0338$ for species e and $\hat{v}_\alpha = 0.0583$ for species D. For species D, which exhibits a higher precision of distribution function, $\Delta_0 f_l(\hat{v}_\alpha = 0.0583)$ remains bellows 0.1 for all provided timesteps and does not exceed 1% when $\Delta t = 2^{-5}$. Considering the high precision of conservation in discrete with a acceptable timestep $\Delta t = 2^{-5}$, the L01jd2 scheme is a good approximation of the fully kinetic model for situations with large mass disparity.
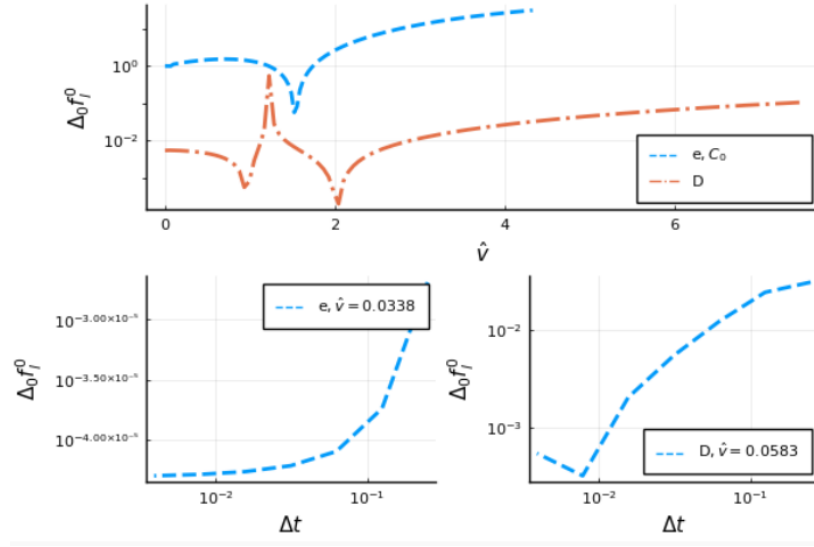
Figure 19: e-D temperature equilibration with enforcing conservation when solved by L01jd2 with fixed timestep, $\Delta t = 2^{-5}$: Criterion C_0 (120) for situation with large mass disparity.

5.3 Electron-Deuterium temperature and momentum equilibration

We consider e-D temperature and momentum equilibration with parameters $m_e = 1/1836$, $m_D = 2$, $-Z_e = Z_D = 1$, $n_e = n_D = 1$, $\hat{u}_e = 0.1$, $\hat{u}_D = -3.162 \times 10^{-2}$, $T_e = 1$ and $T_D = 100$ when $(n_2, N_0) = (7, 7)$. The initial value of $l_{M_1} = 13$, $v_{eth} \approx 0.063$ and $v_{Dth} \approx 0.010$. The expected finial average velocity and temperatures are approximately $u_\infty \approx -9.769 \times 10^{-2}$ and $T_\infty \approx 50.504$, respectively. This case will also be solved by the L01jd2 scheme with a self-adaptive timestep, where the number of time levels is determined to be $N_t = 4877$. In theory, electron-deuterium momentum equilibration will occur first followed by reaching a state of temperature equilibration.
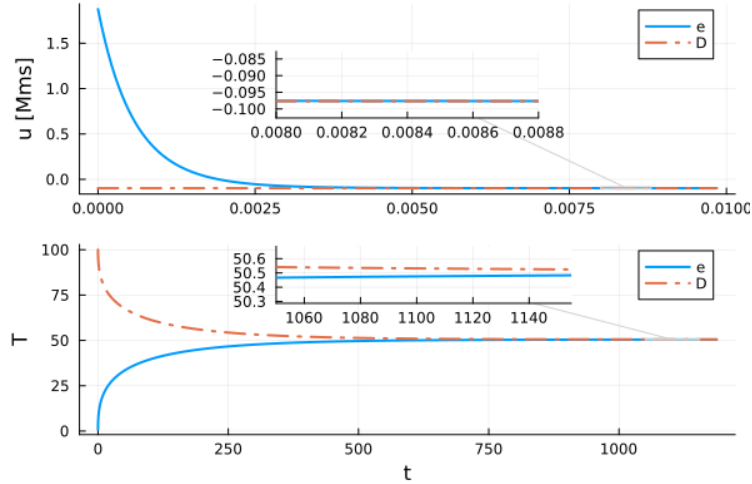

Figure 20: e-D thermal and momentum equilibration with enforcing conservation: Average velocities and temperatures as function of time t when $(n_2, N_0) = (7, 7)$.

The average velocities and temperatures of species e and D are depicted as functions of time t in Fig. 20. The lens in Fig. 20 demonstrates that correct equilibrium values of

35

momentum and temperature are achieved. As anticipated, the characteristic time for momentum relaxation time is significantly shorter than the characteristic time for temperature relaxation during the process of electron-deuterium temperature and momentum equilibration.
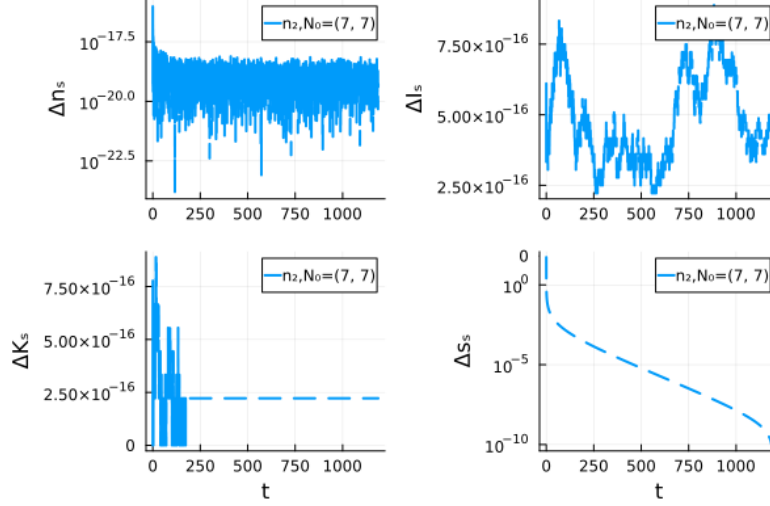

Figure 21: e-D thermal and momentum equilibration with enforcing conservation when $T_e = 1$ and $T_D = 100$: Discrete conservation errors as functions of time when $(n_2, N_0) = (7, 7)$.
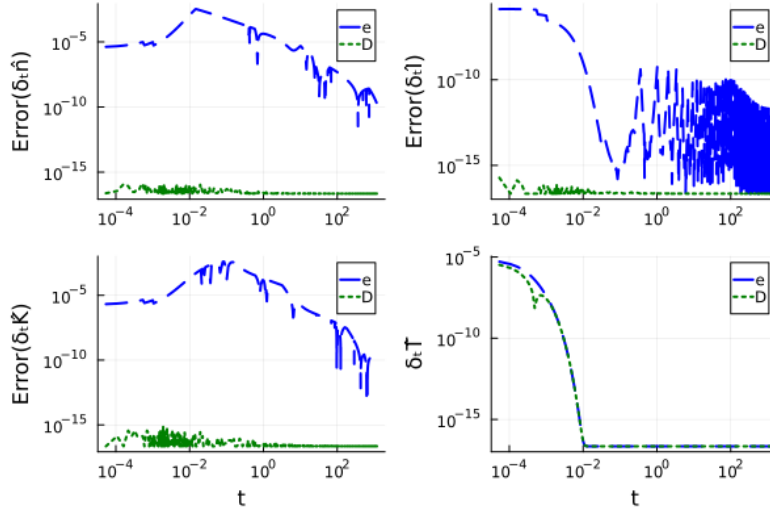

Figure 22: e-D thermal and momentum equilibration with enforcing conservation when $T_e = 1$ and $T_D = 100$: Local errors of $\delta_t \hat{n}$, $\delta_t \hat{I}$, $\delta_t \hat{K}$ and $\delta_t \hat{T}$ as functions of time when $(n_2, N_0) = (7, 7)$.

The time histories of the errors in discrete number density, momentum, energy conservation and entropy conservation are depicted in Fig. 21. As before, mass, momentum and energy conservation (112)-(114) are enforced to the level of round-off error and H-theorem are preserved all the time, as demonstrated in Fig. 21. Fig. 22 illustrates that the local relative errors, $Error(\delta_t \hat{n})$, $Error(\delta_t \hat{I})$, and $Error(\delta_t \hat{K})$ are sufficiently small, satisfying the

convergence criterion for conservation (93) during e-D collision when $(n_2, N_0) = (7, 7)$. As expected, the local relative errors of species D, with its larger mass, are smaller than those of species e. The convergence criterion $\delta_t \hat{T}$ (displayed in Eq. (47)) is approximately valid with high precision, especially when $t \geq 10^{-2}$.

5.4 Three-species (e-D-alpha) thermal equilibration

The finial test case involves the three-species (e-D-$alpha$) thermal equilibration, which is an crucial issue in fusion plasma. Theoretically, the high-energy $alpha$ particles in burning plasma will initially exchange energy with electrons (of comparable v_{th}) and later thermalize with D particles. In this subsection, the subscript "α" represents species $alpha$.

The simulation parameters are $m_e = 1/1836$, $m_D = 2$, $m_\alpha = 4$, $-Z_e = Z_D = 1$, $Z_\alpha = 2$, $n_e = 3$, $n_D = 1$, $n_\alpha = 1$. Initially $\hat{u}_e = \hat{u}_D = \hat{u}_\alpha = 0$, $T_e = T_D = 1$ and $T_\alpha = 1750$, we choose $(n_2, N_0) = (7, 7)$. In this case, $v_{eth} \approx 6.256 \times 10^{-2}$, $v_{Dth} \approx 1.036 \times 10^{-3}$ and $v_{\alpha th} \approx 3.065 \times 10^{-2}$. The characteristic time τ_0 is equivalent to the initial temperature relaxation time between e and D, $\tau_0 = 1/\nu_T^{eD}$, where

$$\nu_T^{eD} \approx 441.72 \times \frac{\sqrt{m_e m_D} \left(Z_e Z_D\right)^2 n_D}{\left(m_e T_D + m_D T_e\right)^{3/2}} \ln \Lambda_{eD} . \tag{123}$$

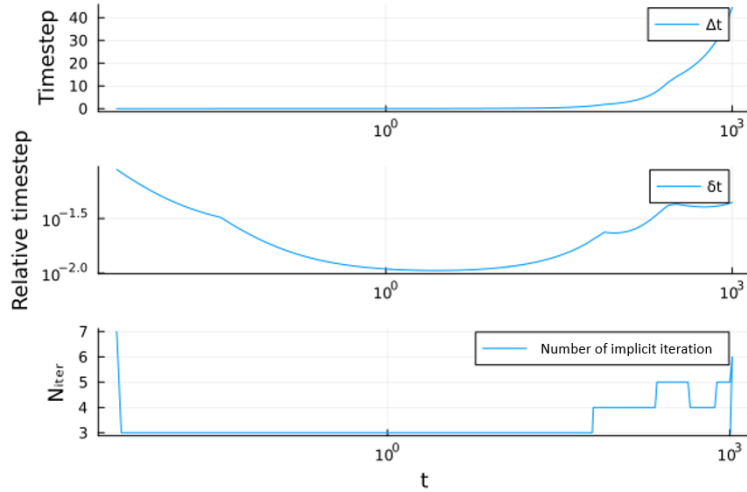The maximum thermal velocity ratio, $v_{eth}/v_{Dth} \sim 60$.

Figure 23: e-D-α thermal equilibration: timestep Δt, the relative timestep δt and number of implicit iterations, N_{iter}, within each time block as functions of time.

This case is solved using a self-adaptive timesteps, with a total of 710 time levels. Fig. 23 illustrates the timestep Δt, the relative timestep δt and number of implicit iterations N_{iter} within each time block as functions of time. Here, the kth timestep and relative timestep are respectively defined as $\Delta t_k = t_{k+1} - t_k$ and $\delta t_k = \Delta t_k/t_{k+1}$. The number of implicit iterations consistently remains below 10, regardless of the timestep and relative timestep. Additionally, due to the effectiveness of the King method, the value of N_{iter} typically does not exceed 5 in most time block.

The temperatures of all species as functions of time t are plotted in Fig. 24. As anticipated, the electrons exhibit a more rapid heating rate comparing to the D particles during the early stage when $t \leq 8$ (lower figure in Fig. 24). However, as electrons and D quickly

heat up while α particles cool down, the preferential interaction switches to one between α and D, ultimately leading to their thermalization together. Eventually, all three species reach the expected equilibrium temperature of $T_\infty = 350.08$ (upper panel in Fig. 24).
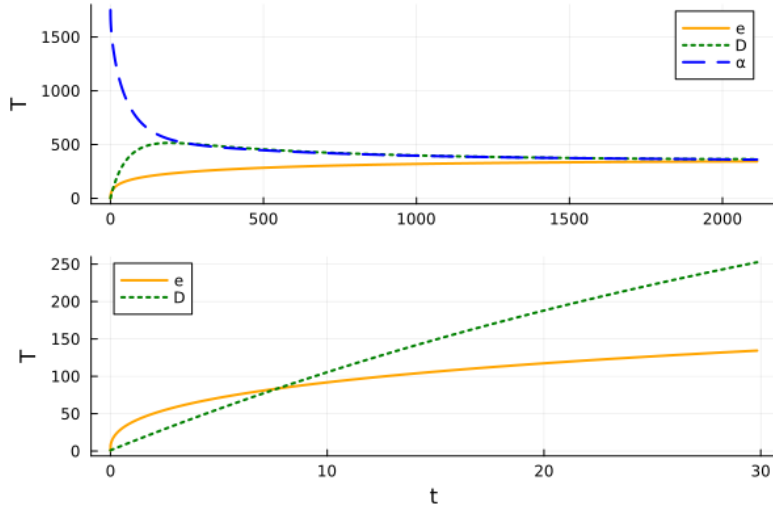

Figure 24: e-D-α thermal equilibration: Temperature of the three species as functions of time (upper) and of e and D at the early time (lower).
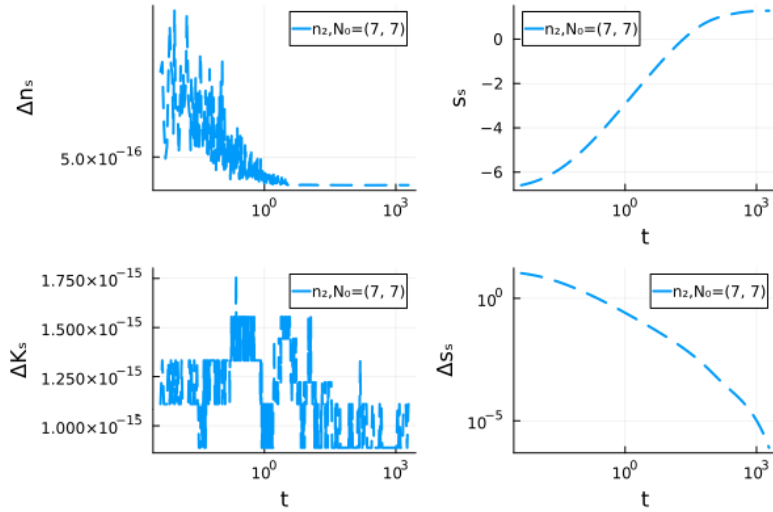

Figure 25: e-D-α thermal equilibration: Discrete conservation errors as functions of time.

The temporal histories of local errors in discrete number density, momentum, energy conservation and entropy conservation are plotted in Fig. 25. As expected, mass and energy conservation represented by Eq. (112) and Eq. (114) are enforced to the level of round-off error. The right-upper subplot of Fig. 25 demonstrates that the entropy satisfies the H-theorem at all time. Δs_s (115) is consistently non-negative, as showed in the right-lower subplot of Fig. 25. In this case, the value of δs_s is about -7.87. The total local relative errors of $\delta_t \hat{n}$ and $\delta_t \hat{K}$ for all species as functions of time t are presented in Fig. 26.

38

It can be observed that the convergence criterion for conservation denoted by Eq. (93) is also satisfied for all sub-processes involving two-species collision process.
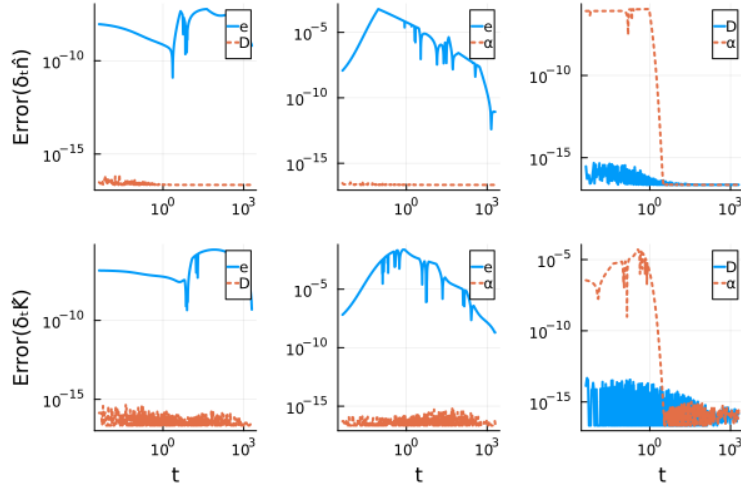

Figure 26: e-D-α thermal equilibration: Local relative errors of $\delta_t \hat{n}$ and $\delta_t \hat{K}$ during all the two-species collision processes as functions of time.

6 Conclusion

In this study, a nonlinear framework (SHE together with KFE) has been introduced for solving the multi-species nonlinear 0D-2V axisymmetric Fokker-Planck-Rosenbluth (FPR) collision equation. In this framework, Legendre polynomial expansion is employed in the angular coordinate, which converges exponentially. KFE, a moment convergence method, is utilized in speed coordinate. This approach ensures mass, momentum, energy conservation and satisfies the H-theorem for plasma simulations with general mass and temperature. An efficient implicit algorithm also has been constructed for weakly anisotropic plasmas based on this framework, employing the nonlinear Shkarofsky's formula of FPR (FPRS) collision operator. The time block technique (TBT) and moment optimization method is utilized in this nonlinear algorithm. Kinetic moments are computed by Romberg integration with high precision. Subsequently, post-step projection to manifold method is applied to enforce the exact conservation of the collision operators.

The high accuracy of our algorithm is demonstrated by solving several typical problems in various non-equilibrium configurations. To handle the large disparate of thermal velocities resulting from the arbitrary disparity of mass and temperature, we incorporate mapping between the different field nodes for collision species. This is also accomplished based on the King function. The fast convergence and high efficiency in handing various challenging problems have showcased the potential of our approach for multi-scale simulation of plasma.

In order to fully realize the potential of the proposed framework for nonlinear, multi-scale plasma systems, it is necessary to expand our approach into a general self-adaptive scheme, including self-adaptive collection of (j, l), number of King function N_{K_a} and field nodes determined by parameter (n_2, N_0) in the speed coordinate. This will be discussed in a future publication. We finally remark that the SHE together with KFE framework is efficient for moderately anisotropic plasma systems, including weakly anisotropic plasmas,

subsonic regions and low supersonic plasmas, while the L01jd2NK scheme is only designed for weakly anisotropic plasmas. The limitation for SHE together with KFE framework is the decreasing convergence rate of SHE as the ratio of average velocity to thermal velocity increases. While the limitation for L01jd2NK scheme is that characteristic parameter in the King function (51) may depend on l when the characteristic group velocity, $\hat{u}_{a_s}$, is large enough and tends to be 1. A general scheme based on the present framework for moderately anisotropic plasma systems will be addressed in our further research.

7 Acknowledgments

Appendix A: King Function

When the velocity space exhibits axisymmetry with $\hat{\mathbf{u}}_a = \hat{u}_a \mathbf{e}_z$, the Gaussian function will be:

$$\mathscr{G}\left(\hat{v}, \mu\right) \;=\; \frac{\hat{n}_a}{\left(\hat{v}_{ath}\right)^3} e^{-\left[(\hat{\mathbf{v}} - \hat{u}_a \mathbf{e}_z)/\hat{v}_{ath}\right]^2}. \tag{124}$$

The Gaussian function can be expanded using Legendre polynomials as:

$$\mathscr{G}\left(\hat{v}, \mu\right) \;=\; \sum_{l=0}^{l_M} \mathscr{G}_l\left(\hat{v}\right) P_l\left(\mu\right) . \tag{125}$$

The lth-order amplitude, $\mathscr{G}_l\left(\hat{v}\right)$ can be calculated by the inverse transformation of Eq. (125), reads:

$$\mathscr{G}_l\left(\hat{v}\right) \;=\; \int_{-1}^{1} \mathscr{G}\left(\hat{v}, \mu\right) P_l(\mu) \mathrm{d}\mu, \quad l \in 0, 1, \cdots, l_M . \tag{126}$$

Substitute Eq. (124) into the equation above, and after a tedious derivation process, one can obtain:

$$\mathscr{G}_l\left(\hat{v}\right) \;=\; \frac{\hat{n}_a}{\left(\hat{v}_{ath}\right)^3} \sum_{m=0}^{l} C_{G_l} \frac{1}{\hat{\xi}_a^{m+1}} \left[(-1)^m e^{-\left(\frac{\hat{v} - \hat{u}_a}{\hat{v}_{ath}}\right)^2} - (-1)^l e^{-\left(\frac{\hat{v} + \hat{u}_a}{\hat{v}_{ath}}\right)^2} \right] . \tag{127}$$

Here, $\hat{\xi}_a = 2\hat{v}\hat{u}_a/\hat{v}_{ath}^2$ and

$$C_{G_l} \;=\; \frac{2l+1}{2} \frac{1}{2^m m!} \frac{(l+m)!}{(l-m)!} . \tag{128}$$

The lth-order King function (51) is in direct proportion to $\mathscr{G}_l$, reads:

$$\mathcal{K}_l\left(\hat{v}; \hat{u}_a, \hat{v}_{ath}\right) \;=\; \sqrt{\frac{1}{2\pi}} \frac{1}{\hat{n}_a} \mathscr{G}_l\left(\hat{v}\right) . \tag{129}$$

The new function introduced in Sec. 3.2.1, King function (51) has the following properties. When $\hat{v} \to \infty$, the King function will be:

$$\lim_{\hat{v} \to \infty} \mathcal{K}_l \left(\hat{v}; \iota, \sigma \right) \rightarrow 0 . \tag{130}$$

When $\xi = 2\iota \hat{v}/\sigma^2 \to 0$, the King function has the following asymptotic behaviour:

$$\lim_{\xi \to 0} \mathcal{K}_l \left(\hat{v}; \iota, \sigma \right) = \sqrt{\frac{1}{2\pi}} \frac{\mathrm{e}^{-\sigma^{-2}\left(\hat{v}^2 + \iota^2\right)}}{(2l-1)!!} \frac{\xi^l}{\sigma^3} \left[1 + \sum_{k=1}^{\infty} \frac{1}{2^l l!} \frac{(2l-1)!!}{(2l+2k+1)!!} \xi^{2k} \right] . \tag{131}$$

In particular, $\xi \equiv 0$ gives:

$$\mathcal{K}_l \left(\hat{v}; \iota, \sigma \right) \stackrel{\xi=0}{=\!=\!=} \delta_l^0 \sqrt{\frac{1}{2\pi}} \frac{1}{\sigma^3} \mathrm{e}^{-\sigma^{-2}\left(\hat{v}^2 + \iota^2\right)} . \tag{132}$$

Here, δ_l^0 is the Kronecker symbol.

Appendix B: Normalized FPRS collision operator

Before presenting the expanded form of the normalized FPRS collision operator, we firstly calculate the derivatives of amplitudes of normalized Rosenbluth potential functions with respect to the speed coordinate $\hat{v}_{ab}$. The partial derivatives in axisymmetric velocity space can be formulated as:

$$\frac{\partial}{\partial \hat{v}_{ab}} \hat{H}_L \left(\hat{v}_{ab}, t \right) = \frac{1}{2L+1} \frac{1}{\hat{v}_{ab}^2} \left[-(L+1)I_{L,L} + (L)J_{L+1,L} \right] , \tag{133}$$

$$\frac{\partial}{\partial \hat{v}_{ab}} \hat{G}_L \left(\hat{v}_{ab}, t \right) = \frac{(L-1)I_{L,L} - (L)J_{L-1,L}}{(2L-1)(2L+1)} - \frac{(L+1)I_{L+2,L} - (L+2)J_{L+1,L}}{(2L+1)(2L+3)} . \tag{134}$$

Similarly, the second partial derivative of $\hat{G}_L$ with respect to $\hat{v}_{ab}$ is:

$$\frac{\partial^2}{\partial \hat{v}_{ab}^2} \hat{G}_L \left(\hat{v}_{ab}, t \right) = C_{G_L}^n \left(I_{L,L} + J_{L-1,L} \right) + C_{G_L}^p \left(I_{L+2,L} + J_{L+1,L} \right) . \tag{135}$$

Here, the coefficients $C_{G_L}^n$ and $C_{G_L}^p$ are given by:

$$C_{G_L}^n = -\frac{L(L-1)}{(2L-1)(2L+1)}, \quad C_{G_L}^p = \frac{(L+1)(L+2)}{(2L+1)(2L+3)} . \tag{136}$$

Similarly, analytical expressions for the first two derivatives of $\hat{f}_l(\hat{v}, t)$ with respect to $\hat{v}$ can be derived based on Eq. (52).

Substituting the distribution function (20), Eq. (24) and Rosenbluth potentials (26) into the normalized FPRS collision operator (14), simplifying the result by combining the like terms yields the normalized FPRS collision operator in axisymmetric velocity space:

$$\hat{\mathfrak{C}}_{ab} \left(\hat{\mathbf{v}}, t \right) = 4\pi \sum_{i=0}^{9} \hat{\mathscr{S}}_i . \tag{137}$$

The zero-order effect term resulting from the normalized background distribution func-

tion, $\hat{F}$, in the collision term can be formulated as:

$$\hat{\mathscr{S}}_0 = m_M \sum_{L=0}^{l_{max}} \hat{F}_L(\hat{v}_{ab}, t) P_L \times \sum_{l=0}^{l_{max}} \hat{f}_l(\hat{v}, t) P_l . \tag{138}$$

The first-order effect terms resulting from $\hat{H}_L$ will be:

$$\hat{\mathscr{S}}_1 = C_{\hat{H}} \sum_{L=0}^{l_{max}} P_L \frac{\partial}{\partial \hat{v}_{ab}} \hat{H}_L \times \sum_{l=0}^{l_{max}} P_l \frac{\partial}{\partial \hat{v}} \hat{f}_l, \tag{139}$$

$$\hat{\mathscr{S}}_2 = C_{\hat{H}} \frac{1}{\hat{v}_{ab}} \sum_{L=1}^{l_{max}} \hat{H}_L P_L^1 \times \frac{1}{\hat{v}} \sum_{l=1}^{l_{max}} \hat{f}_l P_l^1 . \tag{140}$$

Another first-order effect term, $\hat{\mathscr{S}}_3$, will be zero due to the azimuthal derivatives is zero. Specifically, when $m_a = m_b$, the coefficient $C_{\hat{H}}$ provided in Eq. (15) will be zero, resulting in $\hat{\mathscr{S}}_1 = \hat{\mathscr{S}}_2 \equiv 0$ as well. Similarly, the second-order effect terms related to $\hat{G}_L$ will be:

$$\hat{\mathscr{S}}_4 = C_{\hat{G}} \sum_{L=0}^{l_{max}} P_L \frac{\partial^2}{\partial \hat{v}_{ab}^2} \hat{G}_L \times \sum_{l=0}^{l_{max}} P_l \frac{\partial^2}{\partial \hat{v}^2} \hat{f}_l, \tag{141}$$

$$\hat{\mathscr{S}}_5 = 2C_{\hat{G}} \frac{1}{\hat{v}_{ab}} \sum_{L=1}^{l_{max}} \left(\frac{\hat{G}_L}{\hat{v}_{ab}} - P_L \frac{\partial}{\partial \hat{v}_{ab}} \hat{G}_L \right) \times \frac{1}{\hat{v}} \sum_{l=1}^{l_{max}} \left(\frac{\hat{f}_l}{\hat{v}} - P_l \frac{\partial}{\partial \hat{v}} \hat{f}_l \right) P_l^1, \tag{142}$$

$$\hat{\mathscr{S}}_7 = C_{\hat{G}} \frac{1}{\hat{v}_{ab}} \sum_{L=0}^{l_{max}} \left(P_L^{1,2} \frac{\hat{G}_L}{\hat{v}_{ab}} + P_L \frac{\partial \hat{G}_L}{\partial \hat{v}_{ab}} \right) \times \frac{1}{\hat{v}} \sum_{l=0}^{l_{max}} \left(P_l^{1,2} \frac{\hat{f}_l}{\hat{v}} + P_l \frac{\partial \hat{f}_l}{\partial \hat{v}} \right), \tag{143}$$

$$\hat{\mathscr{S}}_9 = C_{\hat{G}} \sum_{L=0}^{l_{max}} \left(P_L^{1,\mu} \frac{\hat{G}_L}{\hat{v}_{ab}^2} + P_L \frac{1}{\hat{v}_{ab}} \frac{\partial \hat{G}_L}{\partial \hat{v}_{ab}} \right) \times \sum_{l=0}^{l_{max}} \left(P_l^{1,\mu} \frac{\hat{f}_l}{\hat{v}^2} + P_l \frac{1}{\hat{v}} \frac{\partial \hat{f}_l}{\partial \hat{v}} \right), \tag{144}$$

where the coefficient $C_{\hat{G}}$ provided in Eq. (15) and coefficients

$$P_l^{1,\mu} = \frac{\mu}{\sqrt{1-\mu^2}} P_l^1, \quad P_l^{1,2} = P_l^2 + P_l^{1,\mu} . \tag{145}$$

The remaining second-order effect terms vanish, $\hat{\mathscr{S}}_6 = \hat{\mathscr{S}}_8 = 0$. As demonstrated by equations above, the FPRS collision operator (137) is generally a nonlinear model.

In particular, when the system is spherical symmetric in velocity space, the collision effect becomes independent of the angular coordinate of velocity space. Therefore, the normalized FPRS collision operator (give in Eq. (137)) will be:

$$\hat{\mathscr{S}}_0(\hat{\mathbf{v}}, t) = m_M \hat{F}_0(\hat{v}_{ab}, t) \times \hat{f}_0(\hat{v}, t), \tag{146}$$

$$\hat{\mathscr{S}}_1(\hat{\mathbf{v}}, t) = C_{\hat{H}} \frac{\partial}{\partial \hat{v}_{ab}} \hat{H}_0 \times \frac{\partial}{\partial \hat{v}} \hat{f}_0, \tag{147}$$

$$\hat{\mathscr{S}}_4(\hat{\mathbf{v}}, t) = C_{\hat{G}} \frac{\partial^2}{\partial \hat{v}_{ab}^2} \hat{G}_0 \times \frac{\partial^2}{\partial \hat{v}^2} \hat{f}_0, \tag{148}$$

$$\hat{\mathscr{S}}_7(\hat{\mathbf{v}}, t) = \hat{\mathscr{S}}_9 = C_{\hat{G}} \frac{1}{\hat{v}_{ab}} \frac{\partial}{\partial \hat{v}_{ab}} \hat{G}_0 \times \frac{1}{\hat{v}} \frac{\partial}{\partial \hat{v}} \hat{f}_0 . \tag{149}$$

42

The remaining first-order effect terms and second-order effect terms will be zero, $\hat{\mathscr{S}}_2 = \hat{\mathscr{S}}_3 = \hat{\mathscr{S}}_5 = \hat{\mathscr{S}}_6 = \hat{\mathscr{S}}_8 = 0$.

For self-collision process, the mass ratio $m_M \equiv 1$ and thermal velocity ratio $v_{abth} \equiv 1$. Therefore, the coefficients (give in Eq. (15)) will remain constants, reads:

$$C_{\hat{H}} = 0, \quad C_{\hat{G}} = 1/2 \ . \tag{150}$$

The normalized FPRS collision operator (give in Eqs. (137)-(149)) can be further simplify to a self-collision operator by substituting $\hat{F}_L$ and $\hat{v}_{ab}$ with $\hat{f}_l$ and $\hat{v}$ respectively.

References

[1] M. N. Rosenbluth, W. M. MacDonald, and D. L. Judd, "Fokker-planck equation for an inverse-square force," *Physical Review*, vol. 107, no. 1, pp. 1–6, 1957.

[2] W. T. Taitano, L. Chacón, A. N. Simakov, and K. Molvig, "A mass, momentum, and energy conserving, fully implicit, scalable algorithm for the multi-dimensional, multi-species Rosenbluth-Fokker-Planck equation," *Journal of Computational Physics*, vol. 297, pp. 357–380, 2015.

[3] I. P. Shkarofsky, "Cartesian Tensor Expansion of the Fokker–Planck Equation," *Canadian Journal of Physics*, vol. 41, no. 11, pp. 1753–1775, 1963.

[4] I. P. Shkarofsky, T. W. Johnston, M. P. Bachynski, and J. L. Hirshfield, "The Particle Kinetics of Plasmas," *American Journal of Physics*, vol. 35, pp. 551–552, 6 1967.

[5] L. D. Landau, "The kinetic equation in the case of Coulomb interaction," *Zh. Eksper. i Theoret. Fiz. 7 (2)*, 1937.

[6] A. A. Vlasov, "THE VIBRATIONAL PROPERTIES OF AN ELECTRON GAS," *Soviet Physics Uspekhi*, vol. 10, pp. 721–733, 6 1968.

[7] V. L. Boltzmann, "Weitere Studien uber das Warmegleichgewicht unter Gas-molekulen," *Wissenschaftliche Abhandlungen*, 1872.

[8] J. Chang and G. Cooper, "A practical difference scheme for Fokker-Planck equations," *Journal of Computational Physics*, vol. 6, pp. 1–16, 8 1970.

[9] W. T. Taitano, L. Chacón, and A. N. Simakov, "An adaptive, conservative 0D-2V multispecies Rosenbluth-Fokker-Planck solver for arbitrarily disparate mass and temperature regimes," *Journal of Computational Physics*, vol. 318, pp. 391–420, 2016.

[10] A. G. Thomas, M. Tzoufras, A. P. Robinson, R. J. Kingham, C. P. Ridgers, M. Sherlock, and A. R. Bell, "A review of Vlasov-Fokker-Planck numerical modeling of inertial confinement fusion plasma," *Journal of Computational Physics*, vol. 231, no. 3, pp. 1051–1079, 2012.

[11] A. R. Bell, A. P. Robinson, M. Sherlock, R. J. Kingham, and W. Rozmus, "Fast electron transport in laser-produced plasmas and the KALOS code for solution of the Vlasov-Fokker-Planck equation," *Plasma Physics and Controlled Fusion*, vol. 48, no. 3, 2006.

[12] T. W. Johnston, "Cartesian tensor scalar product and spherical harmonic expansions in boltzmann's equation," *Physical Review*, vol. 120, no. 4, pp. 1103–1111, 1960.

[13] I. P. Shkarofsky, "Expansion of the relativistic Fokker-Planck equation including non-linear terms and a non-Maxwellian background," *Physics of Plasmas*, vol. 4, no. 7, pp. 2464–2481, 1997.

[14] R. J. Kingham and A. R. Bell, "An implicit Vlasov-Fokker-Planck code to model non-local electron transport in 2-D with magnetic fields," *Journal of Computational Physics*, vol. 194, no. 1, pp. 1–34, 2004.

[15] A. G. Thomas, R. J. Kingham, and C. P. Ridgers, "Rapid self-magnetization of laser speckles in plasmas by nonlinear anisotropic instability," *New Journal of Physics*, vol. 11, 2009.

[16] A. P. Robinson, M. Sherlock, and P. A. Norreys, "Artificial collimation of fast-electron beams with two laser pulses," *Physical Review Letters*, vol. 100, no. 2, pp. 1–4, 2008.

[17] M. Tzoufras, A. R. Bell, P. A. Norreys, and F. S. Tsung, "A Vlasov-Fokker-Planck code for high energy density physics," *Journal of Computational Physics*, vol. 230, no. 17, pp. 6475–6494, 2011.

[18] M. Tzoufras, A. Tableman, F. S. Tsung, W. B. Mori, and A. R. Bell, "A multi-dimensional Vlasov-Fokker-Planck code for arbitrarily anisotropic high-energy-density plasmas," *Physics of Plasmas*, vol. 20, no. 5, 2013.

[19] S. Z. Wu, H. Zhang, C. T. Zhou, S. P. Zhu, and X. T. He, "Kinetic model for energy deposition in fast ignition," in *EPJ Web of Conferences*, vol. 59, 2013.

[20] S. Mijin, F. Militello, S. Newton, J. Omotani, and R. J. Kingham, "Kinetic and fluid simulations of parallel electron transport during equilibria and transients in the scrape-off layer," *Plasma Physics and Controlled Fusion*, vol. 62, no. 9, 2020.

[21] M. Krook and T. T. Wu, "Exact solutions of the Boltzmann equation," *Physics of Fluids*, vol. 20, no. 10, pp. 1589–1596, 1977.

[22] A. R. Bell, R. G. Evans, and D. J. Nicholas, "Elecron energy transport in steep temperature gradients in laser-produced plasmas," *Physical Review Letters*, vol. 46, no. 4, pp. 243–246, 1981.

[23] J. P. Matte and J. Virmont, "Electron Heat Transport down Steep Temperature Gradients," *Physical Review Letters*, vol. 49, pp. 1936–1939, 12 1982.

[24] I. P. Shkarofsky, M. M. Shoucri, and V. Fuchs, "Numerical solution of the Fokker-Planck equation with a dc electric field," *Computer Physics Communications*, vol. 71, no. 3, pp. 269–284, 1992.

[25] F. Alouani-Bibi, M. M. Shoucri, and J. P. Matte, "Different Fokker-Planck approaches to simulate electron transport in plasmas," *Computer Physics Communications*, vol. 164, no. 1-3, pp. 60–66, 2004.

[26] B. Zhao, G. Y. Hu, J. Zheng, and Y. Ding, "Simulations of nonlocal electron transport in cylindrical and spherical thermal waves," *High Energy Density Physics*, vol. 28, no. April, pp. 1–6, 2018.

[27] S. Wu, C. Zhou, S. Zhu, H. Zhang, and X. He, "Relativistic kinetic model for energy deposition of intense laser-driven electrons in fast ignition scenario," *Physics of Plasmas*, vol. 18, 2 2011.

[28] L. Pareschi, G. Russo, and G. Toscani, "Fast Spectral Methods for the Fokker-Planck-Landau Collision Operator," *Journal of Computational Physics*, vol. 165, no. 1, pp. 216–236, 2000.

[29] F. Filbet and L. Pareschi, "A Numerical Method for the Accurate Solution of the Fokker–Planck–Landau Equation in the Nonhomogeneous Case," *Journal of Computational Physics*, vol. 179, pp. 1–26, 6 2002.

[30] A. Pataki and L. Greengard, "Fast elliptic solvers in cylindrical coordinates and the Coulomb collision operator," *Journal of Computational Physics*, vol. 230, no. 21, pp. 7840–7852, 2011.

[31] M. Askari and H. Adibi, "Meshless method for the numerical solution of the Fokker–Planck equation," *Ain Shams Engineering Journal*, vol. 6, pp. 1211–1216, 12 2015.

[32] Morton K. W. and Mayyers David, *Numerical Solution of Partial Differential Equations*, vol. 54. Cambridge University Press, 2005.

[33] R. Li, Y. Ren, and Y. Wang, "Hermite spectral method for Fokker-Planck-Landau equation modeling collisional plasma," *Journal of Computational Physics*, vol. 434, 6 2021.

[34] W. H. Press, S. A. Teukolsky, W. T. Verrerlling, and F. B. P., *Numerical Recipes*. No. 9, Cambridge University Press, 2007.

[35] W. T. Taitano, D. A. Knoll, and L. Chacón, "Charge-and-energy conserving moment-based accelerator for a multi-species Vlasov-Fokker-Planck-Ampère system, part II: Collisional aspects," *Journal of Computational Physics*, vol. 284, pp. 737–757, 3 2015.

[36] W. T. Taitano, L. Chacón, and A. N. Simakov, "An equilibrium-preserving discretization for the nonlinear Rosenbluth–Fokker–Planck operator in arbitrary multi-dimensional geometry," *Journal of Computational Physics*, vol. 339, pp. 453–460, 2017.

[37] D. Daniel, W. T. Taitano, and L. Chacón, "A fully implicit, scalable, conservative nonlinear relativistic Fokker–Planck 0D-2P solver for runaway electrons," *Computer Physics Communications*, vol. 254, p. 107361, 2020.

[38] R. Courant, K. Friedrichs, and H. Lewy, "Über die partiellen Differenzengleichungen der mathematischen Physik," in *Kurt Otto Friedrichs*, pp. 53–95, Boston, MA: Birkhäuser Boston, 1986.

[39] Y. Saad, *Iterative Methods for Sparse Linear Systems, Second Edition*. Society for Industrial and Applied Mathematics, 2003.

[40] O. Larroche, "Kinetic simulations of fuel ion transport in ICF target implosions," *The European Physical Journal D - Atomic, Molecular and Optical Physics*, vol. 27, pp. 131–146, 11 2003.

[41] Hairer E., Wanner G., and Lubich C., *Geometric Numerical Integration*, vol. 31 of *Springer Series in Computational Mathematics*. Berlin/Heidelberg: Springer-Verlag, 2006.

[42] B. Moore and S. Reich, "Backward error analysis for multi-symplectic integration methods," *Numerische Mathematik*, vol. 95, no. 4, pp. 625–652, 2003.

[43] S. Reich, "Backward error analysis for numerical integrators," *SIAM Journal on Numerical Analysis*, vol. 36, no. 5, pp. 1549–1570, 1999.

[44] G. Liu, *An Introduction to Meshfree Methods and Their Programming*. Springer-Verlag, 2005.

[45] C. Rackauckas and Q. Nie, "DifferentialEquations.jl–a performant and feature-rich ecosystem for solving differential equations in Julia," *Journal of Open Research Software*, vol. 5, no. 1, 2017.

[46] F. L. Bauer, "Algorithm 60: Romberg integration," *Communications of the ACM*, vol. 4, p. 255, 6 1961.

[47] E. Hairer, "Backward error analysis for multistep methods," *Numerische Mathematik*, vol. 84, no. 2, pp. 199–232, 1999.

[48] J. D. Huba, *NRL PLASMA FORMULARY*. NRL, 2011.

[49] Y. Wang, J. Xiao, X. Rao, P. Zhang, Y. Adil, and G. Zhuang, "Relaxation model for a homogeneous plasma with spherically symmetric velocity space," 2024.

[50] S. I. Braginskii, "Transport Processes in a Plasma," *Reviews of Plasma Physics*, vol. 1, p. 205, 1 1965.

[51] R. E. Robson and K. F. Ness, "Velocity distribution function and transport coefficients of electron swarms in gases: Spherical-harmonics decomposition of Boltzmanns equation," *Physical Review A*, vol. 33, no. 3, pp. 2068–2077, 1986.

[52] A. Sunahara, J. A. Delettrez, C. Stoeckl, R. W. Short, and S. Skupsky, "Time-Dependent Electron Thermal Flux Inhibition in Direct-Drive Laser Implosions," *Physical Review Letters*, vol. 91, no. 9, pp. 1–4, 2003.

[53] A. S. Joglekar, B. J. Winjum, A. Tableman, H. Wen, M. Tzoufras, and W. B. Mori, "Validation of OSHUN against collisionless and collisional plasma physics," *Plasma Physics and Controlled Fusion*, vol. 60, no. 6, 2018.

[54] G. Arfken and Y. K. Pan, "Mathematical Methods for Physicists (Second Edition)," *American Journal of Physics*, vol. 39, pp. 461–461, 4 1971.

[55] B. Fornberg, "Calculation of weights in finite difference formulas," *SIAM Review*, vol. 40, no. 3, pp. 685–691, 1998.

[56] N. Wiener, "Tauberian theorems," *The Annals of Mathematics*, vol. 33, p. 1, 1 1932.

[57] D. C.-L. Fong and M. Saunders, "LSMR: An Iterative Algorithm for Sparse Least-Squares Problems," *SIAM Journal on Scientific Computing*, vol. 33, pp. 2950–2971, 1 2011.

[58] S. J. Wright and J. N. Holt, "An inexact Levenberg-Marquardt method for large sparse nonlinear least squres," *The Journal of the Australian Mathematical Society. Series B. Applied Mathematics*, vol. 26, pp. 387–403, 4 1985.

[59] C. Kanzow, N. Yamashita, and M. Fukushima, "Levenberg-Marquardt methods with strong local convergence properties for solving nonlinear equations with convex constraints," *Journal of Computational and Applied Mathematics*, vol. 172, pp. 375–397, 12 2004.

[60] S. I. Braginskii, "Transport phenomena in a completely ionized two-temperature plasma," *J. Exptl. Theoret. Phys. (U.S.S.R.)*, vol. 6, no. 33, pp. 459–472, 1958.

[61] B. Fornberg, *A Practical Guide to Pseudospectral Methods*. Cambridge University Press, 1 1996.